The Astrophysical Journal, 921:74 (18pp), 2021 November 1 https://doi.org/10.3847/1538-4357/ac1ba5

Numerical Modeling and Physical Interplay of Stochastic Turbulent Acceleration for Nonthermal Emission Processes

Sayan Kundu[1], Bhargav Vaidya[1], and Andrea Mignone[2]
[1] Discipline of Astronomy, Astrophysics and Space Engineering, Indian Institute of Technology, Indore, Madhya Pradesh, 453552, India
sayan.astronomy@gmail.com
[2] Dipartimento di Fisica Generale, Universita degli Studi di Torino Via Pietro Giuria 1, I-10125 Torino, Italy
Received 2021 June 15; revised 2021 August 5; accepted 2021 August 5; published 2021 November 2

Abstract

Particle acceleration is a ubiquitous phenomenon in astrophysical and space plasma. Diffusive shock acceleration (DSA) and stochastic turbulent acceleration (STA) are known to be the possible mechanisms for producing very highly energetic particles, particularly in weakly magnetized regions. An interplay of different acceleration processes along with various radiation losses is typically observed in astrophysical sources. While DSA is a systematic acceleration process that energizes particles in the vicinity of shocks, STA is a random energizing process, where the interaction between cosmic ray particles and electromagnetic fluctuations results in particle acceleration. This process is usually interpreted as a biased random walk in energy space, modeled through a Fokker–Planck equation. In the present work, we describe a novel Eulerian algorithm, adopted to incorporate turbulent acceleration in the presence of DSA and radiative processes like synchrotron and inverse Compton emission. The developed framework extends the hybrid Eulerian−Lagrangian module in a full-fledged relativistic Magneto-hydrodynamic (RMHD) code PLUTO. From our validation tests and case studies, we showcase the competing and complementary nature of both acceleration processes. Axisymmetric simulations of an RMHD jet with this extended hybrid framework clearly demonstrate that emission due to shocks is localized, while that due to turbulent acceleration originates in the backflow and is more diffuse, particularly in the high-energy X-ray band.

Unified Astronomy Thesaurus concepts: Non-thermal radiation sources (1119); Computational methods (1965); Plasma astrophysics (1261); Magnetohydrodynamical simulations (1966); Shocks (2086)

1. Introduction

From giving a universal power-law trend to the cosmic ray spectrum to explaining the observed emission features of various astrophysical sources, the particle acceleration process plays a crucial role in shaping our understanding of the nature of various space and astrophysical phenomena. Several observations require particles to be accelerated to very high energies in order to explain the energetics in different astrophysical sources. Due to high electrical conductivity, astrophysical plasma is incapable of sustaining a global electric field, making it challenging to energize particles in this scenario. Particle acceleration processes provide an alternative way to accelerate particles in the absence of a global electric field. The existing literature (Blandford 1994; Kirk et al. 1994; Melrose 1996) suggests three main approaches to accelerate charged particles in an astrophysical plasma environment: diffusive shock acceleration (DSA), coherent electric field acceleration, and stochastic turbulent acceleration (STA).

In Fermi (1949), Fermi first gave a proper mechanism for accelerating charged particles to explain the cosmic ray spectrum and the possible origin of high-energy cosmic ray particles. The mechanism considers relativistic particles getting scattered by moving inhomogeneities, mainly various plasma waves (MHD waves for highly relativistic cosmic ray particles; Parker 1955; Sturrock 1966; Kulsrud & Ferrari 1971), and gaining energy (accelerate) in a randomized manner. This process is known as the STA process. The randomness in the acceleration makes this process inefficient to energize particles, as suggested by the emission timescales observed in various astrophysical sources. Nevertheless, STA is considered to be an important source of turbulence damping in plasma and because of the omnipresence of turbulence in various astrophysical sources, STA has been invoked in order to explain the particle acceleration process in solar flares (Petrosian 2012), the corona above the accretion disk of compact objects (Dermer et al. 1996; Liu et al. 2004; Belmont et al. 2008; Vurm & Poutanen 2009), supernova remnants (Bykov & Fleishman 1992; Kirk et al. 1996; Ferrand & Marcowith 2010; Marcowith & Casse 2010), gamma-ray bursts (Schlickeiser & Dermer 2000), emission from blazars (see Asano & Hayashida 2018 and references therein), radio lobes of active galactic nucleus (AGN) jets (O'Sullivan et al. 2009), and the diffuse X-ray emission from AGN jets (Fan et al. 2008), along with Fermi bubbles of galaxies (Mertsch & Petrosian 2019) and the radio halos of galaxy clusters (Brunetti & Lazarian 2007; Donnert & Brunetti 2014). Recently STA has also been suggested as a candidate source for the spectral gradient observed in galaxy clusters (Rajpurohit et al. 2020).

That said, DSA gives a proper framework in which particles can interact with the magnetic inhomogeneities in a way that could only increase the particles' energy (Bell 1978; Drury 1983; Blandford & Eichler 1987; Malkov & Drury 2001). Due to its efficiency, DSA has been used to describe the particle acceleration process in various astrophysical systems, for example in interplanetary heliospheric shocks (Jokipii et al. 2007; Perri & Zimbardo 2015), shock waves of supernova remnants (Bell 2014), stellar bow shocks (Rangelov et al. 2019), oblique shocks in AGN jets (Meli & Biermann 2013), and radio relics of galaxy clusters (Kang et al. 2017; van Weeren et al. 2017; Zimbardo & Perri 2017). Though DSA is more efficient compared to the STA mechanism, it is believed to only give rise to localized

emission, where STA is thought to produce large-scale diffusive emission (Fan et al. 2008).

To study these particle acceleration processes in various astrophysical systems, a numerical approach is imperative because of the multiscale nature of the astrophysical plasma. The numerical study of plasma systems can broadly be categorized into different classes. One is direct computation, mainly known as the Particle in Cell (PIC) method, in which the Newton−Lorenz force law is solved along with Maxwell's equations describing the dynamical evolution of the electric and magnetic field (Giacalone & Ellison 2000; Nishikawa et al. 2007; Spitkovsky 2008; Sironi & Spitkovsky 2011). This first principle approach has been taken by various researchers to study particle acceleration processes (Comisso & Sironi 2018; Wong et al. 2020; Marcowith et al. 2020). The next numerical scheme studies the plasma by solving the Vlasov equation for particle distribution evolution along with Maxwell's equations (Palmroth et al. 2018). This scheme provides the advantage to study various plasma behaviors distinctly. This approach also enables us to study particle acceleration processes in different physical settings. Similar to this approach, another approach is often taken to study the particle acceleration process in the quasi-linear approximation, in which a Fokker −Planck equation is solved in order to evolve the cosmic ray spectrum due to interaction with magneto-hydrodynamic (MHD) waves (Miniati 2001; Donnert & Brunetti 2014; Winner et al. 2019; Vazza et al. 2021).

Another numerical procedure studies the plasma in the fluid regime, also known as the MHD regime. This numerical procedure assumes plasma to be sufficiently collisional. That is why this procedure is incapable of capturing the physics of particle acceleration, because collisions would make them follow a Maxwellian distribution, which is in contrast to the observed power-law trend for the distribution of the accelerated particles. Though the fluid approach fails to capture the particle acceleration process, it provides the background for the particles to interact with various MHD waves and accelerate. Recently some research has been devoted to combine the fluid and the PIC approaches (Bai et al. 2015) to study the DSA (Mignone et al. 2018). The final numerical method uses a Monte Carlo technique to study particle acceleration by shock waves (Achterberg & Krulls 1992; Baring et al. 1994; Marcowith & Kirk 1999; Wolff & Tautz 2015) and turbulence (Giacalone & Jokipii 1999; Teraki & Asano 2019). Among all of the numerical techniques available, the PIC method has an advantage (Ostrowski 1988; Ellison et al. 1990; Ellison & Double 2002; Lemoine & Pelletier 2003; Baring 2004; Niemiec & Ostrowski 2006) over all other techniques because PIC not only can model the particle acceleration process, it can also determine the self-generated magnetic turbulence, and treat them self-consistently with the cosmic ray particles. But the disadvantage of the PIC technique is that it is computationally very expensive (Ellison et al. 2013), and in order to bypass this problem other numerical techniques are used. Among them, the kinetic test particle approach is one of the most efficient because it can easily be incorporated with multiscale simulations.

As most of the sources of particle acceleration act simultaneously in different regions of astrophysical sources, it is imperative to develop a framework that can study such a region to understand role of individual acceleration process. In this work, we use the kinetic test particle approach to study the competing and complementary actions of DSA and STA. Other complementary approaches have focused on studying the role either of the acceleration processes individually; for example, Miniati et al. (2001), Miniati (2003), and Donnert & Brunetti (2014) have demonstrated the role of STA in large-scale galaxy clusters.

Recently, the existing Lagrangian particle module developed by Vaidya et al. (2018) in the PLUTO Code (Mignone et al. 2007) has been applied to AGN jets at kiloparsec scales to study the impact of instabilities and subsequent shocks on particle acceleration and nonthermal emission (Borse et al. 2021; Mukherjee et al. 2021). In the present work, we extend this Lagrangian framework by incorporating the STA process to study the effect of both DSA and STA along with their roles in shaping the emission structure in astrophysical sources. In this context, a macroparticle is a Lagrangian entity that moves along with the fluid and collects an ensemble of real particles (e.g., leptons) that are distributed in 1D momentum space.

The paper is organized as follows. In Section 2, we discuss the fundamental theory and necessary equations to describe the STA process. In Section 3, we propose and describe a numerical algorithm to solve the cosmic ray transport equation. We validate our algorithm and discuss its accuracy in Section 4. We analyze the STA process in the presence and absence of shocks in Section 5 and also discuss the role of several STA parameters through applications to test situations. Section 6 discusses our findings and summarizes this work.

2. Turbulent Particle Acceleration: Theory

This paper aims to study the effect of MHD turbulence and shocks on cosmic ray transport and their effect on the spectral signature of various astrophysical systems. The process of interaction between cosmic ray particles and turbulent plasma is stochastic in nature. Due to the random nature of the interaction, the energy of a cosmic ray particle follows a biased random walk, which causes the particle distribution to follow a diffusion equation (Tverskoĭ 1967):

$$\frac{\partial f_0}{\partial t} = \frac{1}{p^2}\frac{\partial}{\partial p}\left(p^2 D_{pp}\frac{\partial f_0}{\partial p}\right) = \frac{\partial}{\partial p}\left(D_{pp}\frac{\partial f_0}{\partial p}\right) + \frac{2D_{pp}}{p}\frac{\partial f_0}{\partial p}, \quad (1)$$

where, f_0 is the particle distribution function that depends on time t and momentum p. D_{pp} is the diffusion coefficient in momentum space. The above equation resembles a Fokker–Planck equation (Blandford & Eichler 1987). In a magnetized medium, charged cosmic rays are also prone to lose their energy via various radiative and adiabatic losses. Inclusion of these loss effects along with the random interactions with turbulent magnetic fields results in the evolution of the distribution of relativistic cosmic ray particles as follows

(Webb 1989)

$$\nabla_\mu(u^\mu f_0 + q^\mu) + \frac{1}{p^2}\frac{\partial}{\partial p} \times\left[-\frac{p^3}{3} f_0 \nabla_\mu u^\mu + \langle \dot{p}\rangle_L f_0 - \Gamma_{visc} p^4 \tau \frac{\partial f_0}{\partial p} - p^2 D_{pp}\frac{\partial f_0}{\partial p} - p(p^0)^2 \dot{u}_\mu q^\mu\right] = 0. \tag{2}$$

The various terms of the equation are described below:

1. $\nabla_\mu(u^\mu f_0 + q^\mu)$ represents the change in f_0 due to the spatial transport. q^μ is the spatial diffusion flux, and u^μ is the bulk four-velocity;
2. $\frac{p^3}{3} f_0 \nabla_\mu u^\mu$ defines the energy loss due to adiabatic expansion;
3. $\langle \dot{p}\rangle_L f_0$ describes the radiative losses, such as synchrotron and various inverse Compton (IC) processes;
4. $\Gamma_{\rm visc} p^4 \tau \frac{\partial f_0}{\partial p}$ is the particle acceleration term due to fluid shear (Rieger & Duffy 2019);
5. $p^2 D_{pp} \frac{\partial f_0}{\partial p}$ represents the Fermi II order particle acceleration or STA process (see Equation (1));
6. $p(p^0)^2 \dot{u}_\mu q^\mu$ originates because of the frame transformation.

Following Vaidya et al. (2018), we neglect the spatial diffusion flux q^μ as well as the acceleration due to frame transformation (i.e., terms 1 and 6). Also, acceleration due to shear flow ($\Gamma_{\rm visc} = 0$) is not considered in the present study. Furthermore, the omission of the spatial diffusion term is compromised by the inclusion of a momentum-independent escape term in Equation (2); (Achterberg & Krulls 1992), so that Equation (2) takes the form,

$$\nabla_\mu(u^\mu f_0) + \frac{1}{p^2}\frac{\partial}{\partial p}\left[-\frac{p^3}{3} f_0 \nabla_\mu u^\mu + \langle \dot{p}\rangle_L f_0 - p^2 D_{pp}\frac{\partial f_0}{\partial p}\right] = -\frac{f_0}{T_{\rm esc}}, \tag{3}$$

where $T_{\rm esc}$ is the escape timescale. The above equation is same one used in Vaidya et al. (2018) to update the spectral distribution of a single macroparticle with the additional contributions related to Fermi II order acceleration and the escape term.

Note that, for relativistic flows, the convective derivative can be expressed as,

$$u^\mu \nabla_\mu \equiv \gamma\left[\frac{\partial}{\partial t} + v^i \frac{\partial}{\partial x^i}\right] = \frac{d}{d\tau}, \tag{4}$$

where τ is the proper time. Assuming pitch angle isotropy in momentum space (p), the distribution function can be written in terms of the number density of the relativistic particles as $N(p, \tau)dp = 4\pi p^2 f_0 dp$ with $N(p, \tau)$ being the number density of nonthermal particles with momentum between p and $p + dp$. Accordingly Equation (3) can be written as,

$$\frac{dN}{d\tau} + \frac{\partial}{\partial p}\left[-N\nabla^\mu u_\mu \frac{p}{3} + \frac{\langle \dot{p}\rangle_l}{p^2} N - D_{pp}\frac{\partial N}{\partial p} + \frac{2ND_{pp}}{p}\right] = -N\nabla^\mu u_\mu - \frac{N}{T_{\rm esc}}. \tag{5}$$

Transforming the independent variable from momentum (p) to the Lorentz factor (γ) following $p \approx \gamma m_0 c$, with c being the speed of light in a vacuum and m_0 being the mass of the ultra-relativistic cosmic ray particles, Equation (5) can be expressed as (see Equation 11 of Tramacere et al. 2011):

$$\frac{\partial \chi_p}{\partial \tau} + \frac{\partial}{\partial \gamma}[(S + D_A)\chi_p] = \frac{\partial}{\partial \gamma}\left(D\frac{\partial \chi_p}{\partial \gamma}\right) - \frac{\chi_p}{T_{\rm esc}} + Q(\gamma, \tau), \tag{6}$$

where $\chi_p = N/n$, with n being the number density of the fluid at the position of macroparticle, S corresponds to radiative and adiabatic losses, and $D_A = 2D/\gamma^2$ corresponds to the acceleration due to Fermi II order with $D = D_{pp}/m_0^2 c^2$. We also include $Q(\gamma, \tau)$ as a source term in Equation (6), which accounts for a particle injection process from external sources.

A numerical approach to solve Equation (6) without the terms on the right-hand side and D_A has been discussed in an earlier work (Vaidya et al. 2018), along with the particle energization through a first-order Fermi acceleration at shocks. The numerical method for DSA has recently been improved to account for the history of particle spectra by Mukherjee et al. (2021) and will be repeated here for completeness.

The improved version of the DSA routine includes a convolution of the upstream spectra to the downstream region of the shock in an instantaneous steady-state manner. In particular, as the macroparticle crosses the shock, its downstream spectra is updated as follows:

$$\chi_p^{\rm down}(\gamma) \propto \int_{\gamma_{\rm min}}^{\gamma} \chi_p^{\rm up}(\gamma') G(\gamma, \gamma')\frac{d\gamma}{\gamma} \tag{7}$$

where $\chi_p^{\rm up}(\gamma)$ is the distribution function far upstream and $\chi_p^{\rm down}(\gamma)$ is the steady-state downstream distribution function, $G(\gamma, \gamma') = (\gamma/\gamma')^{-m+2}$, with $m = 3r/(r-1)$, and r is the compression ratio. Here, $\gamma_{\rm min}$ is the minimum value of the Lorentz factor obtained from the upstream spectrum. The value of $\gamma_{\rm max}$, the upper limit of the convolution, is evaluated by equating timescales due to radiative losses and various acceleration processes (i.e., DSA and STA; Böttcher & Dermer 2010; Mimica & Aloy 2012; Vaidya et al. 2018). Furthermore, it is also ensured that the Larmor radius of the highest energetic lepton within a macroparticle has a radius equal to or less than one grid cell width. Further details are explicitly mentioned in Vaidya et al. (2018) and Mukherjee et al. (2021).

2.1. Momentum Diffusion Coefficient (D)

The microphysical processes of the turbulent interaction are encapsulated in the transport coefficients of Equation (6). The mathematical form of these transport coefficients due to different interactions of cosmic rays and the turbulent magnetized medium have been derived for Alfvènic turbulence (see, for instance, Schlickeiser 2002; Brunetti & Lazarian 2007; O'Sullivan et al. 2009).

In this work, we will consider STA following a 1D energy spectrum expressed as a power law in terms of the wavevector norm $|\boldsymbol{k}| = k$ with exponent $-q$,

$$W(k) \sim k^{-q}, \tag{8}$$

where $W(k)$ is the turbulent energy spectrum in Fourier space. The momentum diffusion coefficient can therefore be expressed as (Schlickeiser 1989; O'Sullivan et al. 2009)

$$D_{pp} \approx \beta_A^2 \frac{\delta B^2}{B^2}\left(\frac{r_g}{\lambda_{\max}}\right)^{q-1}\frac{p^2c^2}{r_g c} \propto p^q, \tag{9}$$

where p is the momentum of the cosmic ray particles, D_{pp} is the momentum diffusion coefficient, β_A is the Alfvén velocity normalized to the speed of light, B is the mean magnetic field, δB its fluctuations, r_g is the particle gyroradius, and $\lambda_{\max}$ is the maximum correlation length of the turbulent medium.

With the definitions above, the systematic acceleration timescale (t_A) for STA can be written as

$$t_A \approx \beta_A^{-2}\frac{l}{c}, \tag{10}$$

where l (the mean free path of the cosmic ray particle) can be expressed as

$$l \approx \frac{B^2}{\delta B^2}\left(\frac{r_g}{\lambda_{\max}}\right)^{1-q} r_g. \tag{11}$$

Therefore, the acceleration timescale (Equation (10)) in terms of γ could be expressed as

$$t_A \approx \frac{A^2}{2}\rho c (m_0\gamma c^2)^{2-q} B^{q-4}\lambda_{\max}^{q-1}, \tag{12}$$

where $A = B/\delta B$ defines the turbulence level, whose value is set to unity for the present study (O'Sullivan et al. 2009).

2.2. Timescales

The processes described in Equation (6) involve separate timescales due to different radiative losses and the STA process. These timescales can be expressed in terms of the particle Lorentz factor γ as follows:

1. Radiative losses timescale due to IC in the Thompson limit and synchrotron radiation, $t_L \propto 1/\gamma$;
2. Diffusion timescale due to Fermi II order momentum diffusion, $t_D \propto \left(\frac{\gamma}{\gamma_s}\right)^{2-q}$, for the chosen diffusion coefficient $D \propto \left(\frac{\gamma}{\gamma_s}\right)^{q}$. The value of t_D therefore becomes a constant, $t_D = 1/D_0$, with a choice of $q = 2$, where D_0 is the proportionality constant. Here, γ_s defines the scale Lorentz factor, which we have taken to be unity for all of the cases considered in this work;
3. The acceleration timescale $t_A = t_D/2$, estimated from Equation (6) with the acceleration coefficient $D_A = 2D/\gamma$.

These considerations are of crucial importance in devising a numerical scheme for the solution of Equation (6), since an explicit method would demand $\Delta t < \min\{t_L, t_D, t_A\}$ for stability reasons.

3. Turbulent Particle Acceleration: Algorithm

3.1. Numerical Method

Equation (6) is a inhomogeneous, convection-diffusion-like partial differential equation (PDE) with variable coefficients. This equation combines both hyperbolic and parabolic terms. The inhomogeneous character of the equation is attributed to the presence of the source and sink terms.

While various numerical methods for the numerical solution of Equation (6) have been proposed (see, for instance, Chang & Cooper 1970; Winner et al. 2019), here we take a more up-to-date and refined approach based on the employment of Runge–Kutta IMplicit-EXplicit (RK-IMEX) schemes whereby the hyperbolic terms of the PDE are treated using an upwind Godunov-type explicit formalism, while the parabolic (diffusion) term is handled implicitly.

Also, in order to account for the large range of values taken by the particle Lorentz factor γ, we employ a logarithmically spaced grid to provide equal resolution per decade.

To this end, we first introduce a coordinate transformation for the independent coordinate $\gamma \in [\gamma_{\min}, \gamma_{\max}]$ in the following way,

$$\xi(\gamma) = \frac{\log(\gamma/\gamma_{\min})}{\log(\gamma_{\max}/\gamma_{\min})}, \tag{13}$$

where, $\xi \in [0,\ 1]$ is the transformed (logical) coordinate. Equation (6) is then rewritten as

$$\frac{\partial \chi}{\partial \tau} + \xi'\frac{\partial}{\partial \xi}(H\chi) = \xi'\frac{\partial}{\partial \xi}\left[D\xi'\frac{\partial \chi}{\partial \xi}\right] - \frac{\chi}{T_{esc}} + Q \tag{14}$$

where we have dropped the subscript p for ease of notation, and ξ' is the Jacobian of this transformation given by Equation (13),

$$\xi' = \frac{d\xi}{d\gamma} = \frac{1}{\gamma\log(\gamma_{\max}/\gamma_{\min})}, \tag{15}$$

while $H = S + D_A$, from Equation (6).

In order to apply the RK-IMEX scheme, we discretize Equation (14) on a one-dimensional mesh of N points using the method of lines,

$$\frac{d\chi_i}{dt} = \mathcal{A}_i + \mathcal{D}_i + \mathcal{S}_i, \tag{16}$$

so that the original PDE becomes a system of ordinary differential equations at the nodal points $i = i_b, \ldots, i_e$, with $N = i_e - i_b + 1$. In Equation (16), $\mathcal{A}_i$ is the advection term, $\mathcal{D}_i$ is the diffusion term, and $\mathcal{S}_i$ accounts for accounts for source and sink terms.

The advection term $\mathcal{A}_i$ is discretized in a conservative fashion using the nonlinear Van Leer flux limiter scheme (Van Leer 1977),

$$\mathcal{A}_i = -\xi'_i\frac{\mathcal{F}^{\rm adv}_{i+\frac{1}{2}} - \mathcal{F}^{\rm adv}_{i-\frac{1}{2}}}{\Delta\xi}, \tag{17}$$

where the advection flux follows an upwind selection rule,

$$\mathcal{F}^{\rm adv}_{i+\frac{1}{2}} = \begin{cases} H(\gamma_{i+\frac{1}{2}})\chi^L_{i+\frac{1}{2}} & H(\gamma_{i+\frac{1}{2}}) > 0 \\ H(\gamma_{i+\frac{1}{2}})\chi^R_{i+\frac{1}{2}} & H(\gamma_{i+\frac{1}{2}}) < 0. \end{cases} \tag{18}$$

The left and right states $\chi^L_{i+\frac{1}{2}}$ and $\chi^R_{i+\frac{1}{2}}$ are constructed up to second- order accuracy in space using a slope limiter to prevent oscillations around extrema,

$$\chi^L_{i+\frac{1}{2}} = \chi_i + \frac{\delta\chi_i}{2},$$
$$\chi^R_{i+\frac{1}{2}} = \chi_{i+1} - \frac{\delta\chi_{i+1}}{2}, \tag{19}$$

with $\Delta\chi_i$, the harmonic mean slope limiter (Van Leer 1977),

$$\delta\chi_i = \begin{cases} \dfrac{2\Delta\chi_{i+\frac{1}{2}}\Delta\chi_{i-\frac{1}{2}}}{\Delta\chi_{i+\frac{1}{2}} + \Delta\chi_{i-\frac{1}{2}}} & \text{if } \ \Delta\chi_{i+\frac{1}{2}}\Delta\chi_{i-\frac{1}{2}} > 0 \\ 0 & \text{otherwise} \end{cases} \tag{20}$$

where $\Delta\chi_{i\pm\frac{1}{2}} = \pm(\chi_{i\pm1} - \chi_i)$. Note that this scheme is second-order accurate away from discontinuities and that the reconstruction step demands for two ghost zones beyond the active domain cells.

For the diffusion term $\mathcal{D}_i$, we also adopt a conservative formalism and choose a central differencing approach yielding second-order accuracy in the uniform ξ grid:

$$\mathcal{D}_i = \xi'_i \frac{\mathcal{F}^{\rm diff}_{i+\frac{1}{2}} - \mathcal{F}^{\rm diff}_{i-\frac{1}{2}}}{\Delta\xi}, \tag{21}$$

where

$$\mathcal{F}^{\rm diff}_{i+\frac{1}{2}} = (\xi' D(\gamma, t))_{i+\frac{1}{2}} \left(\frac{\chi_{i+1} - \chi_i}{\Delta\xi}\right) \tag{22}$$

is the diffusion flux constructed following a central difference approach.

In the RK-IMEX approach, the advection is carried out explicitly while the diffusion operator and the source terms are handled implicitly. This allows one to overcome the restrictive time step limitation $\Delta t \lesssim \Delta\xi^2/(\xi' D)$ imposed by a typical explicit discretization.

We have implemented two similar approaches for the temporal integration of Equation (16) in the PLUTO code. The first one is the Strong Stability Preserving (SSP) scheme (2, 2, 2) of Pareschi & Russo (2005).

Omitting the subscript i for simplicity,

$$\chi^{(1)} = \chi^{(n)} + \Delta t\alpha\mathcal{D}^{(1)}$$
$$\chi^{(2)} = \chi^{(n)} + \Delta t[\mathcal{A}^{(1)} + (1 - 2\alpha)\mathcal{D}^{(1)} + \alpha\mathcal{D}^{(2)}]$$
$$\chi^{(n+1)} = \chi^{(n)} + \frac{\Delta t}{2}[\mathcal{A}^{(1)} + \mathcal{A}^{(2)} + \mathcal{D}^{(1)} + \mathcal{D}^{(2)}], \tag{23}$$

where Δt is the time step, $\alpha = 1 - 1/\sqrt{2}$.

For the second approach we choose the ARS(2, 2, 2) scheme due to Ascher et al. (1997):

$$\chi^{(1)} = \chi^{(n)} + \Delta t[\alpha\mathcal{A}^{(n)} + \alpha\mathcal{D}^{(1)}]$$
$$\chi^{(n+1)} = \chi^{(n)} + \frac{\Delta t}{2}[\delta\mathcal{A}^{(n)} + (1 - \delta)\mathcal{A}^{(1)}]$$
$$+ \frac{\Delta t}{2}[(1 - \alpha)\mathcal{D}^{(1)} + \alpha\mathcal{D}^{(n+1)}], \tag{24}$$

where $\alpha = 1 - 1/\sqrt{2}$, $\delta = 1 - \frac{1}{2\alpha}$.

Both time-stepping methods require the inversion of two tri-diagonal matrices per step, which we perform following the Thomas algorithm (Press et al. 1992). In the present work, we will only show results from the SSP(2, 2, 2) scheme since results obtained with the ARS(2, 2, 2) are similar. Furthermore, for the sake of comparison, we have also implemented the standard Chang–Cooper algorithm (Chang & Cooper 1970; Park & Petrosian 1996) for solving the Fokker–Planck equation.

3.1.1. Boundary Conditions

In order for our numerical method to operate correctly, boundary conditions (b.c.) must be specified in the guard (or ghost) zones for $i = i_b - 1$, $i_b - 2$ and likewise for $i = i_e + 1$, $i_e + 2$. Two common b.c. have been routinely employed (Marcowith et al. 2020). The first one (zero-particle) is a Dirichlet b.c. requiring the value of the distribution function χ to vanish in the ghost zones. This kind of boundary condition in solving the cosmic ray transport problem is used, for instance, by Winner et al. (2019). Another boundary condition is a Neumann-like condition requiring zero-flux across the boundary interface. This condition has been used, for instance, by Chang & Cooper (1970) to solve the Fokker–Planck equation. The zero-flux b.c. conserves the integral of $\int\chi d\gamma$ (analogous to particle number conservation). For more discussion on the boundary conditions for cosmic ray transport, see Park & Petrosian (1995). Unless otherwise stated, we will employ the zero-flux b.c. to ensure that without the presence of source and sink terms in Equation (6), the total number of particles remains conserved. At the implementation level, we enforce the zero-flux b.c. separately according to the implicit/explicit stage level in our RK-IMEX update:

1. During the implicit diffusion step we impose a zero-gradient b.c.:

$$\begin{cases} \chi^{\rm diff}_i = \chi^{\rm diff}_{i_b} & \text{for } i < i_b \\ \chi^{\rm diff}_i = \chi^{\rm diff}_{i_e} & \text{for } i > i_e \end{cases}, \tag{25}$$

   where $\chi^{\rm diff}$ is the solution array immediately before the implicit step.
2. During the explicit hyperbolic update we impose the reflective condition

$$\begin{cases} \chi^{\rm adv}_i = -\chi^{\rm adv}_{2i_b - i - 1} & \text{for } i < i_b \\ \chi^{\rm adv}_i = -\chi^{\rm adv}_{2i_e - i + 1} & \text{for } i > i_e \end{cases} \tag{26}$$

   together with

$$\mathcal{F}^{\rm adv}_{i_b-\frac{1}{2}} = \mathcal{F}^{\rm adv}_{i_e+\frac{1}{2}} = 0. \tag{27}$$

   In Equation (26) $\chi^{\rm adv}$ represents the solution array immediately before the explicit advection step.

A third b.c. is used to assess the accuracy of our algorithm against a reference or analytical solution. In this case, the value of χ in the ghost zones is set to the corresponding analytical value in those zones, unless otherwise stated.

4. Results: Code Validation Tests

In this section we proceed to assess the accuracy of our newly proposed algorithm. For the accuracy calculation, errors will be computed using the L_1 norm, defined as (Winner et al. 2019):

$$L_1(N) = \frac{\sum_{i=1}^{N} |\chi_i^{\rm ref} - \chi_i^{\rm num}|\ \Delta\gamma_i}{\sum_{i=1}^{N} \chi_i^{\rm ref}\,\Delta\gamma_i}, \tag{28}$$

where N is the number of energy bins. To further ensure that the scheme accuracy is not dominated by the spatial discretization, the increment in N is compensated for by the decrement in Δt such that the ratio $N/\Delta t$ stays constant (Vaidya et al. 2017). In Section 5 all of the tests are performed following the zero-flux boundary prescription. Furthermore all of the simulations in this work are performed using the SSP(2, 2, 2) scheme with Courant number 0.4, unless otherwise specified.

4.1. Simple Advection

We start by considering a simple advection benchmark by setting $S = k\gamma^2$, $D_A = D = 0$ in Equation (6). Here, we consider two cases, owing to two different values of $k = \pm 1$. The analytical solution for the case of $k = -1$ is given by Kardashev (1962) and Sarazin (1999):

$$\chi_p = \begin{cases} N_0\gamma^{-s}(1 - \gamma/\gamma_{\rm cut})^{s-2}, & \gamma \geqslant \gamma_{\rm cut} \\ 0, & \gamma \leqslant \gamma_{\rm cut} \end{cases} \tag{29}$$

where $\gamma_{\rm cut} = 1/\tau$, while for $k = 1$ we do not encounter such discontinuity in the result:

$$\chi_p = N_0\gamma^{-s}(1 + \gamma/\gamma_{\rm cut})^{s-2}. \tag{30}$$

The initial condition consists of a power-law spectrum, $\chi_p(\gamma, 0) = N_0\gamma^{-s}$ with s=3.3. For the numerical calculations, we consider the range of $\gamma \in [10,\ 10^3]$ as our computational domain. We show the evolution of χ_p and the corresponding error for both values of k in Figure 1, using 128 bins and a fixed time step $\Delta\tau = 0.00375$. The top left panel of Figure 1 shows the evolution of χ_p for $k = 1$, while the bottom left panel depicts the same for $k = -1$. The solid curves represent the numerical solutions while the black dotted curves depict the analytical solution at the corresponding time. For $k = 1$, the distribution function follows the analytical results closely, while for $k = -1$ some deviations are observed at a later stage ($\tau = 0.03$) between the analytic and numerical solution, owing to the steepening of the solution (Equation (29)). A convergence test is shown for both cases in the right panel of Figure 1 where we plot the L_1 error as a function of the number of bins. Blue dots and the black dashed curve represent, respectively, the computed L_1 error and a reference for the $1/N^2$ slope. For $k = 1$ (top right), results converge with second-order accuracy for all resolutions, while for $k = -1$ (bottom right) a slight deviation from the second-order convergence can be observed. This discrepancy is attributed to the discontinuous nature of the analytic solution presented in Equation (29).

4.2. Simple Diffusion

Next, we solve Equation (6) in the case of simple diffusion where $S = D_A = 0$ and $D = \gamma^2$. The analytical solution for this case can be written as (Park & Petrosian 1995)

$$\chi_p = \frac{1}{\gamma\sqrt{4\pi\tau}} \exp\left\{-\frac{[\log(\gamma_0/\gamma) + \tau]^2}{4\tau}\right\}. \tag{31}$$

We define the computational domain as $\gamma \in [1,\ 10^6]$ and employ 128 logarithmically spaced bins with a fixed time step $\Delta\tau = 0.0375$. The initial condition is given by the analytical solution (Equation (31)) at $\tau = 1.0$ and $\gamma_0 = 100.0$. The results are shown in Figure 2. The left panel shows the evolution of the distribution function at different times with the solid (black dotted) curve representing the numerical (analytical) solution. In the right panel of Figure 2 the corresponding L_1 error is shown by varying the grid size from 32 to 4096 bins. Here, second-order convergence is observed uniformly at all resolutions.

4.3. Hard-sphere Equations

The next numerical benchmark is intended to verify the correctness of our implementation when source and sink terms are present in the Fokker–Planck equation. Additionally, we also compare our code with the standard Chang–Cooper algorithm (Chang & Cooper 1970). For this purpose, we solve the following Fokker–Planck equation

$$\frac{\partial\chi_p}{\partial\tau} = \frac{\partial}{\partial\gamma}\left(\gamma^2\frac{\partial\chi_p}{\partial\gamma} - \gamma\chi_p(\gamma, \tau)\right) - \theta\chi_p. \tag{32}$$

The analytical solution of the previous equation can be written as (Park & Petrosian 1995),

$$\chi_p = \frac{e^{-\theta\tau}}{\gamma\sqrt{4\pi\tau}} \exp\left\{-\frac{[\log(\gamma_0/\gamma) + 2\tau]^2}{4\tau}\right\}. \tag{33}$$

For the present purpose, we take the inverse escape timescale $\theta = 1$ and the initial particle distribution is obtained by setting $\tau = 1.0$, $\gamma = \gamma_0 = 100.0$ in Equation (33). The computational domain is taken as $\gamma \in [1,\ 10^6]$ using 128 (log-spaced) energy bins and a fixed time step $\Delta\tau = 0.0375$.

Numerical solutions obtained via the Chang–Cooper algorithm (dashed curves) and the SSP(2, 2, 2) algorithm (solid lines) are shown in the left panel of Figure 3 at different times (colors). The analytical solution (dotted lines) is also superposed. The corresponding resolution study is reported in the right panel of the same figure using the L_1 error. From the plots it clearly appears that the Chang–Cooper algorithm converges at a first-order rate while the SSP(2, 2, 2) scheme gives full second-order convergence, so that even at low resolutions the latter yields an error that is already one order of magnitude smaller than the former. At the resolution of $N = 4096$ the SSP method outperforms the Chang–Cooper scheme by more than three orders of magnitude.

Notice that, although we employ a conservative discretization, particle number is not strictly conserved for this test, owing to the chosen boundary condition that allows a nonzero

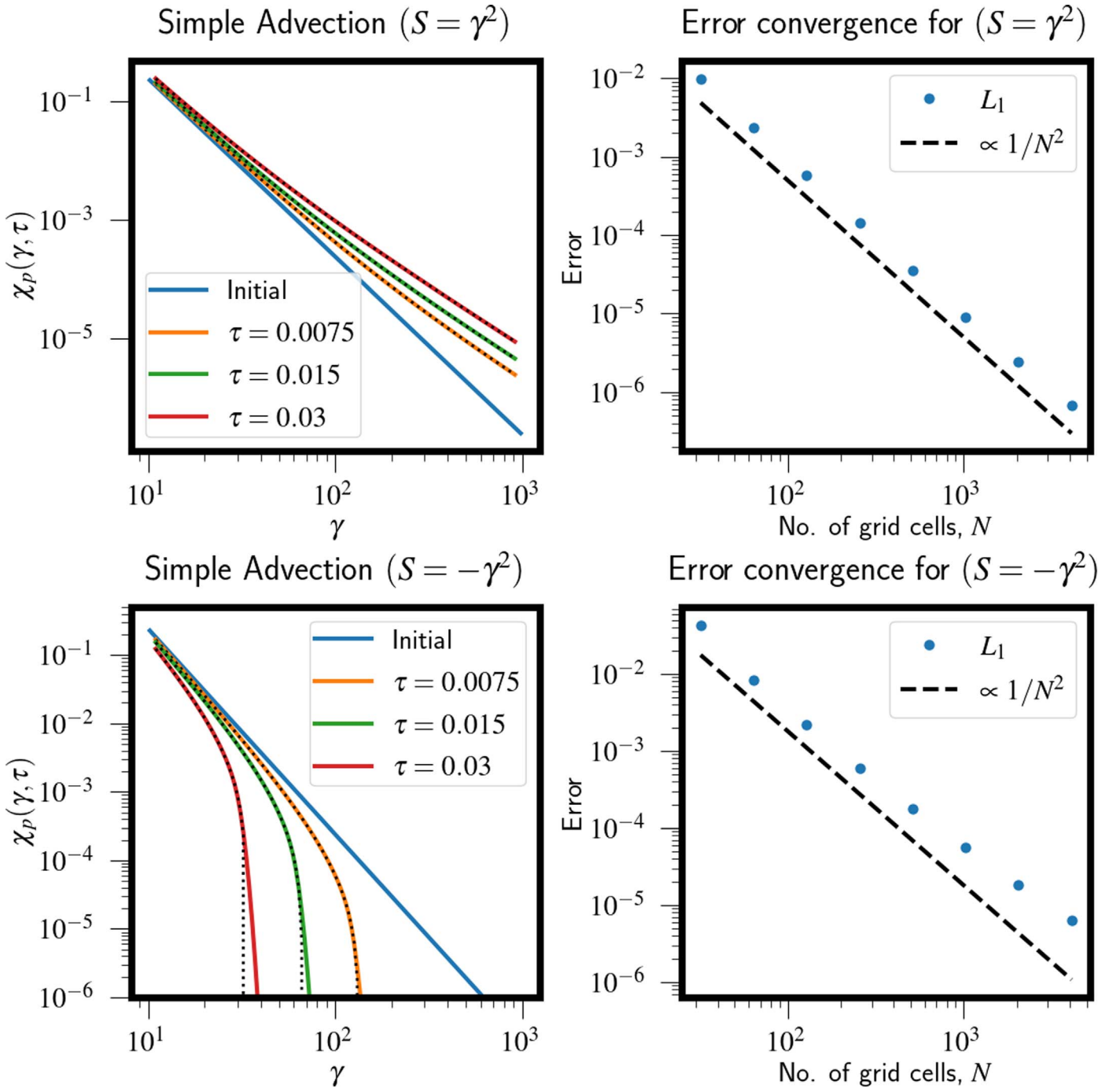

Figure 1. Evolution of the particle distribution function and their corresponding L_1 error for simple advection following the $S = \gamma^2$ (top panel) and $S = -\gamma^2$ (bottom panel) case with the IMEX-SSP algorithm. Left panels: the numerical (solid lines) and analytical (black dotted lines) solutions at different times. Right panel: L1 norm errors at different resolutions (blue dots) and second-order reference slope (dashed lines).

net flux through the endpoints of the computational domain. In order to check particle conservation, we have therefore repeated the same test in absence of a sink term ($\theta = 0$) and by prescribing the zero-flux b.c. (see Section 3.1.1). Results for the previous and current b.c. are shown in Figure 4. It can be observed from the figure that while the integral due to the previous b.c (depicted by green dots) decreases with time, the integral due to the zero-flux b.c. (depicted by black dots) remains constant. This validates the particle number conserving nature of the proposed boundary condition.

4.4. Log-parabolic Nature of Particle Spectra

It has been shown (Massaro et al. 2004, 2006) that the hump structure in the spectral energy distribution (SED) of blazars could be described with a log-parabolic curve, and this log-parabolicity is speculated to have originated from STA (Tramacere et al. 2011). Here, we validate the log-parabolic nature of the particle distribution due to STA, which consequently translates to the log-parabolic nature of the observed SED. In particular, we numerically solve the transport Equation (6), in its conservative form

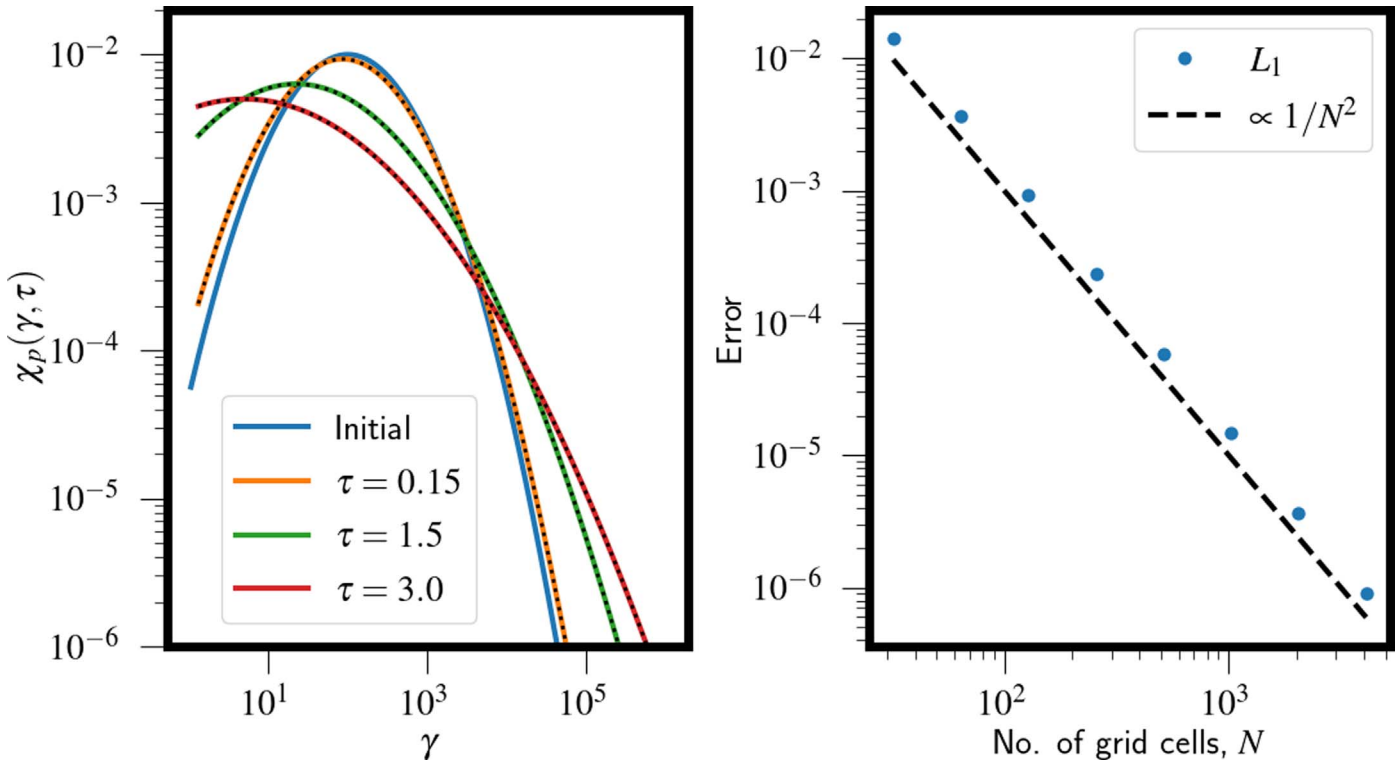

Figure 2. Left: simple diffusion case for different times where solid lines show the numerically computed particle distribution function and the black dotted curves depict the analytical solutions. Right: L_1 error convergence plot for the simple diffusion case with the IMEX-SSP algorithm.

(without source and sink terms), using the zero-flux boundary prescription for STA including synchrotron losses. We choose our grid as $1.0 \leqslant \gamma \leqslant 10^9$ with 5000 computational bins and $\Delta\tau = 0.003$ with the following transport coefficients,

$$S = -C_0\gamma^2 B^2, \;\; D = D_0\gamma^2, \;\; D_A = \frac{2D}{\gamma}, \tag{34}$$

where $C_0 = 1.28 \times 10^{-9}$, and $D_0 = 10^{-4}$ s^{-1} is the diffusion constant. We employ $1/D_0$ as our unit time (t_s).

Here, we consider the one-zone model for the blazar emission (Tramacere et al. 2011) where the geometry of the acceleration region is taken as spherical with radius $R = 5 \times 10^{13}$ cm threaded by a magnetic field $B_{\rm mag}$. In this region, the acceleration is accompanied by the radiative losses. Moreover, in order to solve Equation (6) we consider a mono-energetic initial distribution χ_p corresponding to a total power $L_{\rm inj} = 10^{39}$ erg s^{-1}, where

$$L_{\rm inj} = N_{\rm part}\frac{4}{3}\pi R^3 \int \gamma m_e c^2 \delta(\gamma - \gamma_{\rm inj}) d\gamma, \tag{35}$$

in which $N_{\rm part}$ is the total number of particles injected per unit volume and $\gamma_{\rm inj} = 10.0$. The Dirac delta is approximated with a Gaussian distribution with $\sigma = 0.5$ and $\mu = 10$, and it is shown by the purple solid line in the left panel of Figure 5. Furthermore, Equation (6) is solved by adopting two different magnetic field values $B_{\rm mag} = 1$ G and 0.1 G, and the corresponding distribution of χ_p for time $\tau = 30\, t_s$ is shown in the top left panel of Figure 5.

The numerical solution is shown in the top left panel of Figure 5 for different magnetic field strengths. We point out that the steady-state distribution is expected to have an ultra-relativistic Maxwellian form as described in Equation (A2) in Appendix. This is confirmed in the bottom panel of Figure 5 where we plot χ_p/γ^2 as a function of γ, showing that our results correctly reproduce the γ^2 dependence of the spectrum.

Also, in order to quantify the effects of acceleration and radiative losses on the spectral evolution, we estimate the curvature of the distribution function. The curvature is measured by finding the peak value of the distribution function at each time step, which is also the point at which $t_L = t_A$ (Katarzyński et al. 2006, see also Section 2.2), and subsequently fitting a log-normal curve through 10 points centered around γ_c (the energy at which the maximum occurs). The curvature is then taken as the inverse of the variance of the best fit. In particular, we adopt the fitting curve (Kardashev 1962) as follows:

$$\chi_{\rm fit} = \frac{A}{\gamma\sigma}\exp\left\{-\frac{(\log(\gamma) - \mu - \sigma^2)^2}{4\sigma^2}\right\}, \tag{36}$$

with the curvature parameter defined as $r = 1/(4\sigma^2)$. The fitting curve is a solution to the Fermi II order transport equation (Equation (6) with $S = 0$, $D = \gamma^2$, and $D_A = 2D/\gamma$ without sources and sinks) when $\sigma^2 = \tau$; therefore the evolution of the curvature r goes as $\sim 1/(4\tau)$. In the top right panel of Figure 5 we compare r in the acceleration region (yellow solid line) with r numerically calculated by fitting Equation (36) with the particle distribution, at each time, for different $B_{\rm mag}$ values (red and black dotted lines) .

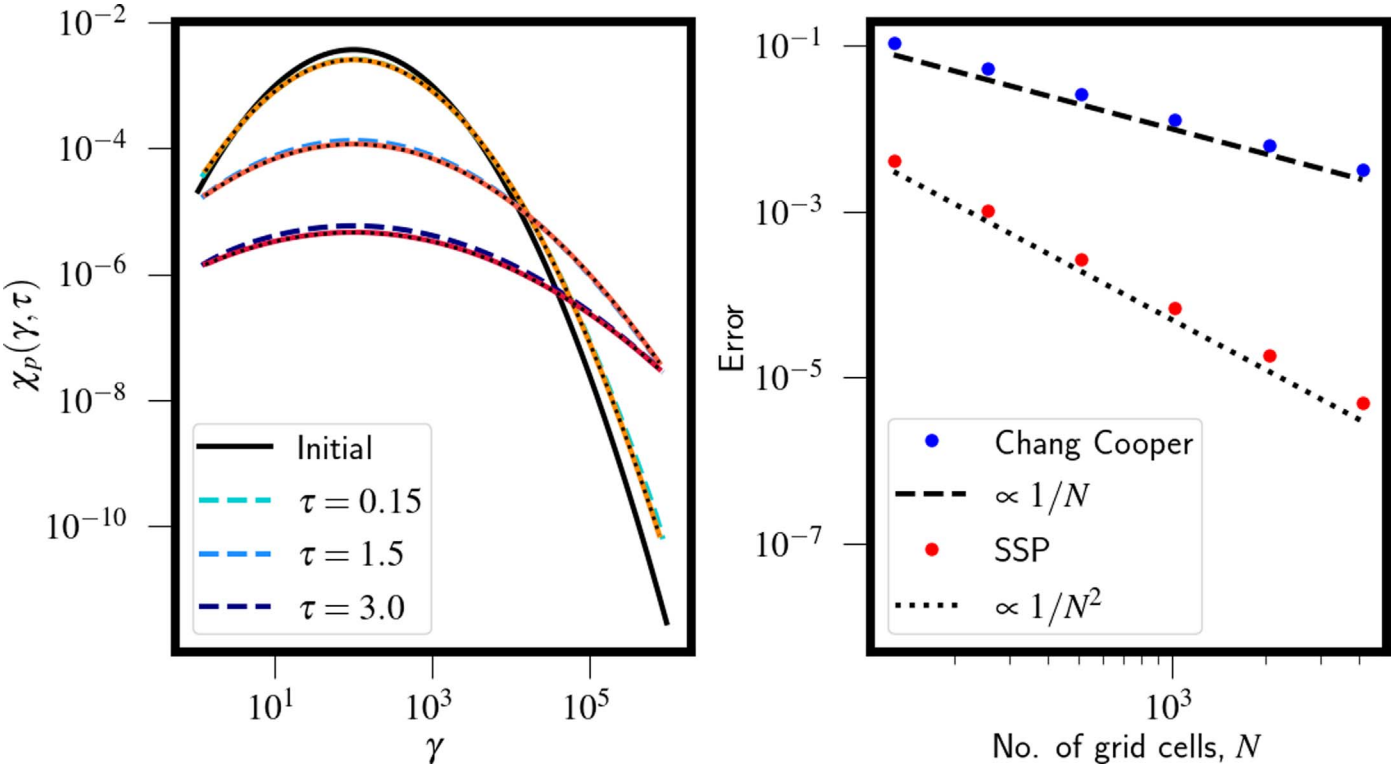

Figure 3. Left: evolution of the particle distribution following Equation (32) with $\theta = 1$. Dashed curves plot results obtained with the Chang–Cooper scheme, and red curves correspond to the SSP(2, 2, 2) scheme. Different shades correspond to different times. Black dotted curves depict the analytical solutions at the corresponding times. Right: L_1-norm error convergence for both Chang–Cooper (blue dots) and SSP(2, 2, 2) (red dots) schemes. Black curves show the reference slopes for the corresponding schemes.

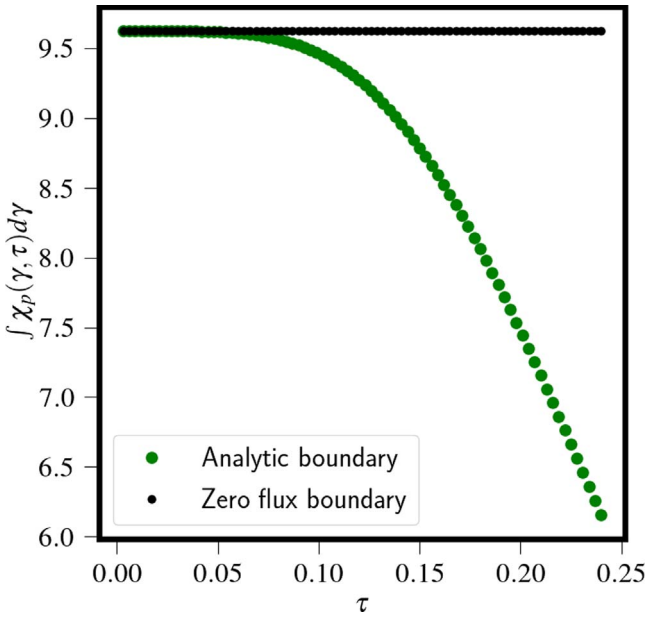

Figure 4. Time evolution of the integral $\int \chi_p(\gamma, \tau)d\gamma$ is shown for the proposed boundary condition (zero-flux boundary) along with the boundary condition where the value of the distribution functions in the ghost zones are computed from the analytic expression (analytic boundary).

Our results show that the fitted curvature initially decays with time as $r \propto t_s/4\tau$, following a trend of curvature in the acceleration region, and a sudden jump of the curvature to the steady value of $r = 0.25$ can be observed. The results therefore confirm that, during the earlier stages, STA dominates the evolution of the particle distribution function and, later, that steady state is reached much faster for stronger magnetic fields, as confirmed by the curvature evolution (black dots in the top right plot of Figure 5).

Summarizing, the numerical benchmarks proposed in this section validate our implementation and demonstrate that the proposed SSP(2, 2, 2) scheme is fully conservative and it provides full second-order accuracy, in contrast to its predecessors (i.e., Chang & Cooper 1970; Winner et al. 2019) with typical first-order accuracy.

5. Effect of Turbulent Acceleration in the Presence of Shocks

In this section, we describe the effect of STA on particle spectra in presence of shocks. In particular, we consider several test situations in which the equations of classical or relativistic MHD are solved using the PLUTO code (Mignone et al. 2007) along with Lagrangian particles to model the nonthermal emission (Vaidya et al. 2018; Mukherjee et al. 2021) in the presence of DSA and radiative losses. To study the effects of STA, the newly developed algorithm (see Section 3) has been incorporated into the Lagrangian framework. The effects of DSA and STA on particle spectra and the subsequent nonthermal emission signatures are compared for various test situations and discussed in the following.

5.1. Nonrelativistic MHD Planar shock

Here, we perform a simulation of a nonrelativistic MHD planar shock interacting with a single macroparticle in a turbulent medium. We solve the 2D ideal MHD equations with

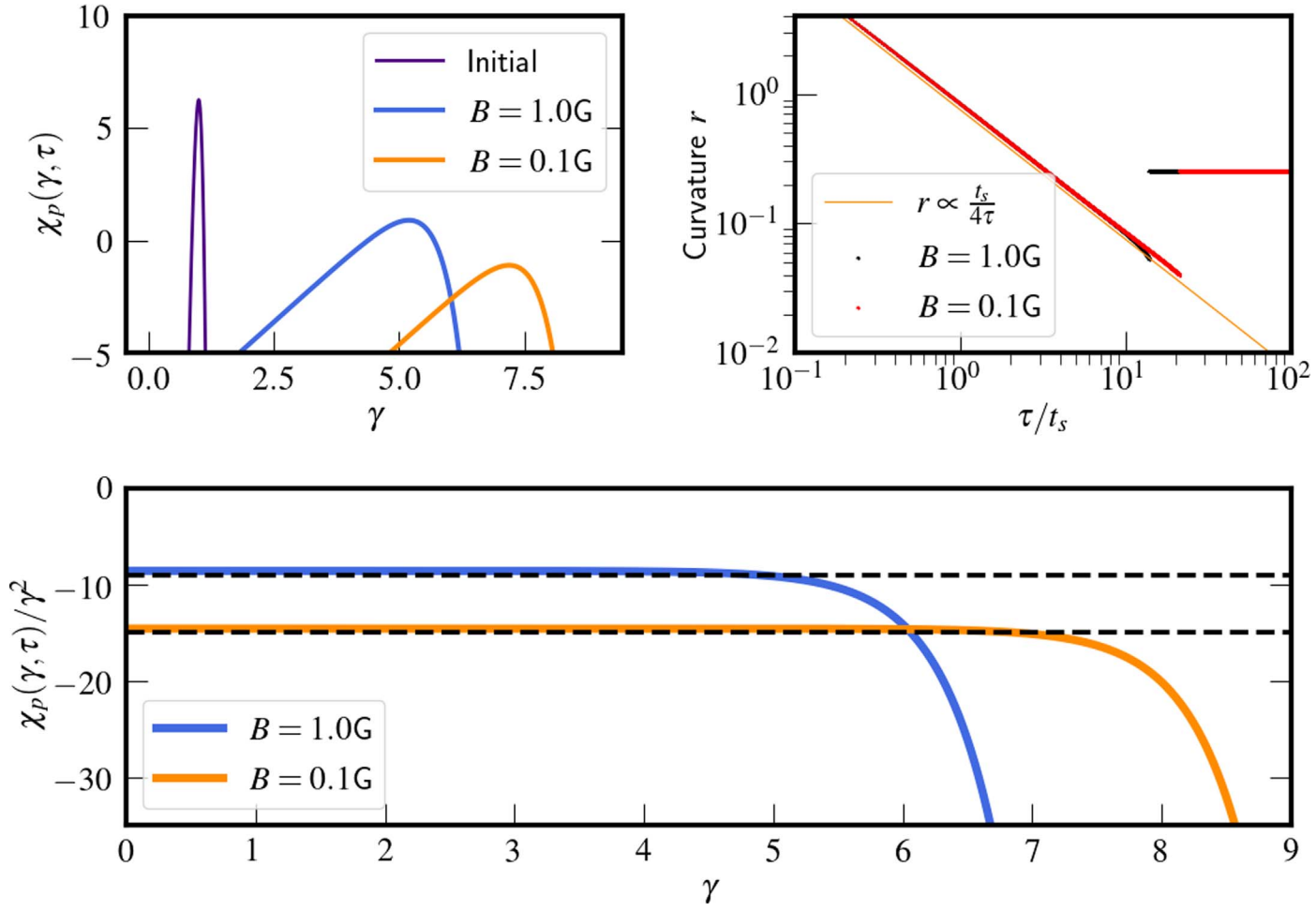

Figure 5. Top left: evolution of the particle distribution function with turbulent acceleration and synchrotron losses with two magnetic field values. Top right: evolution of the curvature of the distribution function fitted with a log-normal density profile (Equation (36)). The analytic solution is shown by the solid orange line. Bottom panel: $\chi_p(\gamma, \tau)/\gamma^2$ as a function of γ at steady state ($\tau = 30\, t_s$), in agreement with Equation (A2). The plot shows an increase as γ^2 (black dashed lines) followed by an exponential cutoff.

an adiabatic equation of state on a Cartesian grid $x \in [0, 40]$ and $y \in [0, 2]$ using 1024×128 grid zones. Initially, we place a shock wave at $x = 1$ that moves toward the increasing x direction. The upstream density and pressure, ρ_u and P_u, are taken as 1 and 10^{-4}, respectively, in dimensionless units. A random density perturbation is added to simulate an inhomogeneous upstream medium. The magnetic field is defined as $\boldsymbol{B} = B_0(\cos\theta, \sin\theta)$, where θ (the obliquity) is the angle between $\boldsymbol{B}$ and the direction of the shock normal. For our purpose, we have considered $\theta = 30°$, while B_0 is computed from the plasma beta, $\beta = 10^2 = 2P_u/B_0^2$.

The physical units adopted for this test are: length $\hat{L}_0$= 100 pc and density $\hat{\rho}_0 = 10^{-2}$ amu, while the unit velocity is taken to be the speed of light c. With this choice, pressure will be given in units of $\hat{P}_0 = 1.5 \times 10^{-5}$ dyne cm^{-2}, the magnetic field in units of $\hat{B}_0 = 1.4 \times 10^{-2}$ G, and time in units of $\hat{\tau}_0 = 326.4$ yr.

The particle is initially located at $(x, y) \equiv (1.5, 1.0)$ with an energy distribution following a steep decreasing power-law profile with index 9. The grid ranges in $10 \leqslant \gamma \leqslant 10^{10}$ using 128 (log-spaced) bins. The particle spectrum (Equation (6)) is evolved accounting for synchrotron, inverse Compton, and adiabatic losses along with the diffusion effect, modeled following the STA timescale (Equation (12)). Additionally, the effect of the shock is captured via the steady-state update convolution, Equation (7). We also vary the index q for various turbulent spectra $W(k) \propto k^{-q}$ in three different scenarios: (1) with only STA and no shock, (2) both shock and STA, and (3) both shock and STA with the latter active only in the downstream region. The value of $\lambda_{\max}$ is taken to be $\hat{L}_0/10^5$ for all of the simulations.

The result in the case of weak turbulence ($q = 2$) is shown in Figure 6 where t_A (see Section 2.2) is independent of γ. The top panel shows the Lagrangian particle position on top of the background gas density distribution at $t = 56.13$ s. The evolution of the particle energy spectra with various radiative losses and different acceleration scenarios is shown in the bottom four panels using different colors (as indicated by the color bar). The upper plot depicts the evolution of the particle spectra for the situation when only DSA is effective. As the shock hits the particle, the spectra become flatter, and radiative and adiabatic losses give rise to a cutoff that gradually shifts from larger values of γ to lower values.

The evolution of the particle spectra due to STA alone is shown in the corresponding right panel. The spectra are now considerably different when compared to the previous case since, owing to turbulence and losses, particle energization occurs continuously rather than just when crossing the shock.

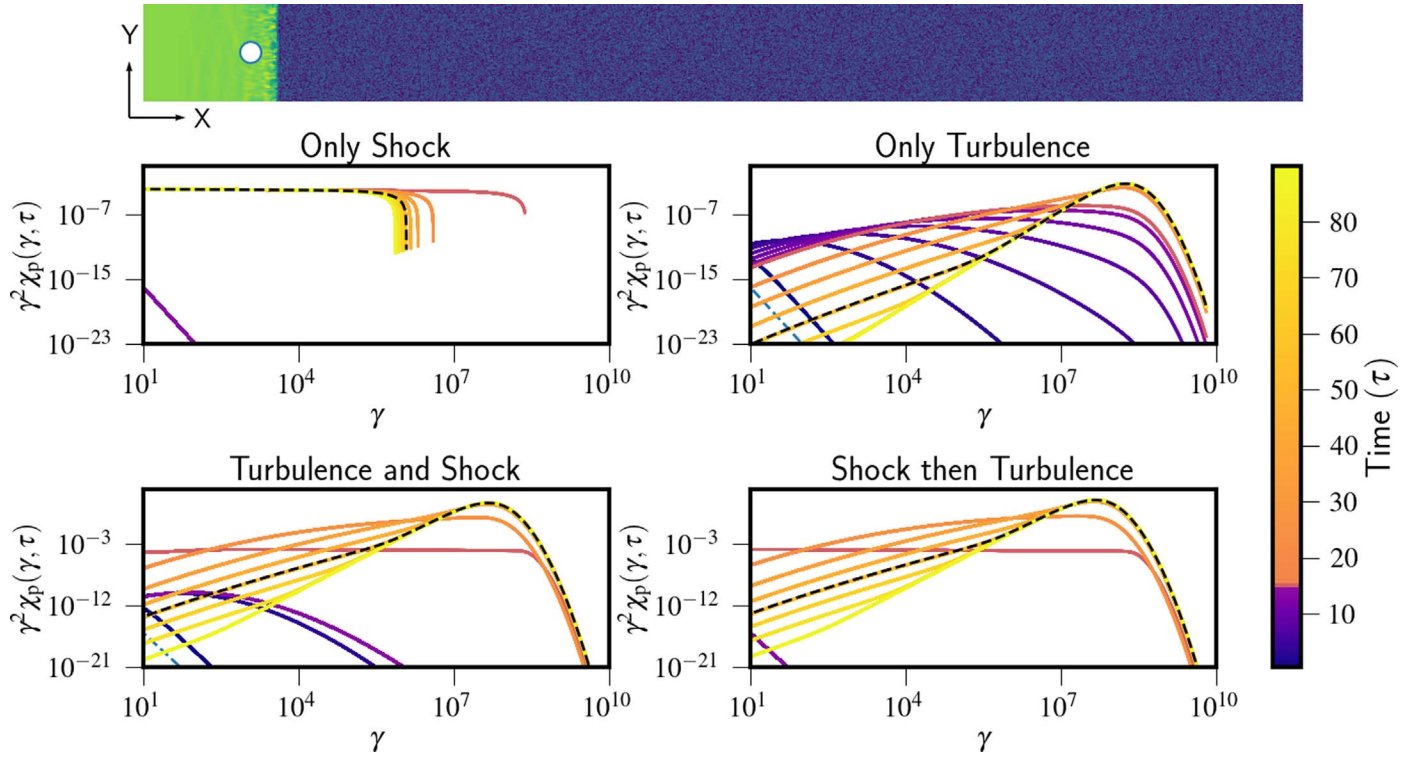

Figure 6. Top section: density map of a fluid with a Lagrangian particle (shown as a white dot). The upstream region is shown in blue, and the downstream region is shown in green. Bottom section: Particle spectra in various scenarios with a $q = 2$ turbulence spectrum. Middle left: particle spectra for the case of only DSA with a compression ratio of 3.89 and various losses. Middle right: in a turbulent medium with various losses but no shock. Bottom left: with the shock of the same compression ratio, turbulence, and various losses. Bottom right: for turbulence present only at the downstream region. The black dashed curve shows the particle energy spectrum for the time when the density map snapshot is taken.

The spectra evolve toward the typical steady state of the ultra-relativistic Maxwellian, as observed in Section 4.4, with a peak value $\gamma_c \sim 10^8$ when $t_A = t_L$. We also notice that the high-energy cutoff does not ever decrease to lower values of γ (as for the pure DSA), but, rather, it settles into a steady state as the result of mutual compensation between losses and STA.

In the bottom left plot, we show the evolution of the energy spectrum in the presence of both a shock and STA. Both the upstream and the downstream are turbulent. In this scenario, the distribution function becomes harder than the initial one owing to the presence of upstream turbulence. The height of the spectrum now considerably increases compared to the previous two cases. Such an increase is primarily due to the subgrid modeling adopted at the shock front: the particle enters the shock with a pre-accelerated spectrum and eventually ends up in the downstream region with a different steady state (when compared to the STA alone case).

Finally, the particle energy evolution for the case in which STA is active only in the downstream region is shown in bottom right panel. As expected, the particle distribution does not significantly change until the particle crosses the shock and then enters in the downstream region where turbulence is active. Here, steady state is attained due to STA. In this sense, the evolution resembles the previous case.

Furthermore notice that, for all of the cases but the pure DSA one, the particle distribution functions eventually seem to achieve steady states of a similar kind. This is expected, as the predicted steady-state spectrum depends on the functional form of the transport coefficients that are not affected by the presence of the shock.

5.1.1. Effect of Turbulence on the Evolution of Particle Spectra

Additionally, in Figure 7 we compare the particle steady-state distribution for turbulent spectra with $q = 5/3$ (top right) and $q = 3/2$ (bottom) with that obtained for $q = 2$ (top left).

The main difference between the acceleration scenarios for turbulent spectra with $q = 2$, on one side, and $q = 5/3$ or $q = 3/2$, on the other, is that the latter achieve a steady state more rapidly because of the dependence of t_A on γ.

Furthermore, the steady-state spectra for $q = 5/3$ and $3/2$ in the case of a shock and STA are not significantly different from the ones computed with STA alone (see the blue and orange solid line in the top right and bottom of Figure 7). Owing to the smaller acceleration timescale, in fact, the spectra for $q = 5/3$ and $3/2$ approach the steady state only when the particle arrives in the upstream region, making the shock injection less effective (see Section 6) compared to the $q = 2$ case. However, for the case where turbulence is present only in the downstream region, shock injection can clearly be observed (solid green line in Figure 7) as no significant turbulent energization took place in the upstream region.

Additionally, we analyze the behavior of γ_c, with various values of B_0, ρ_u, and $\lambda_{\max}$. Analytically the value of γ_c can be calculated by equating t_A to t_L and yielding

$$\gamma_c = \left\{ 2 \times 10^3 \times \frac{\left(\frac{eB\lambda_{\max}}{m_e c^2}\right)^{2-q}}{\rho \lambda_{\max}} \right\}^{\frac{1}{3-q}} . \tag{37}$$

Plots of γ_c computed from simulation data with different values of B , ρ, and $\lambda_{\max}$ are compared in Figure 8 together with the

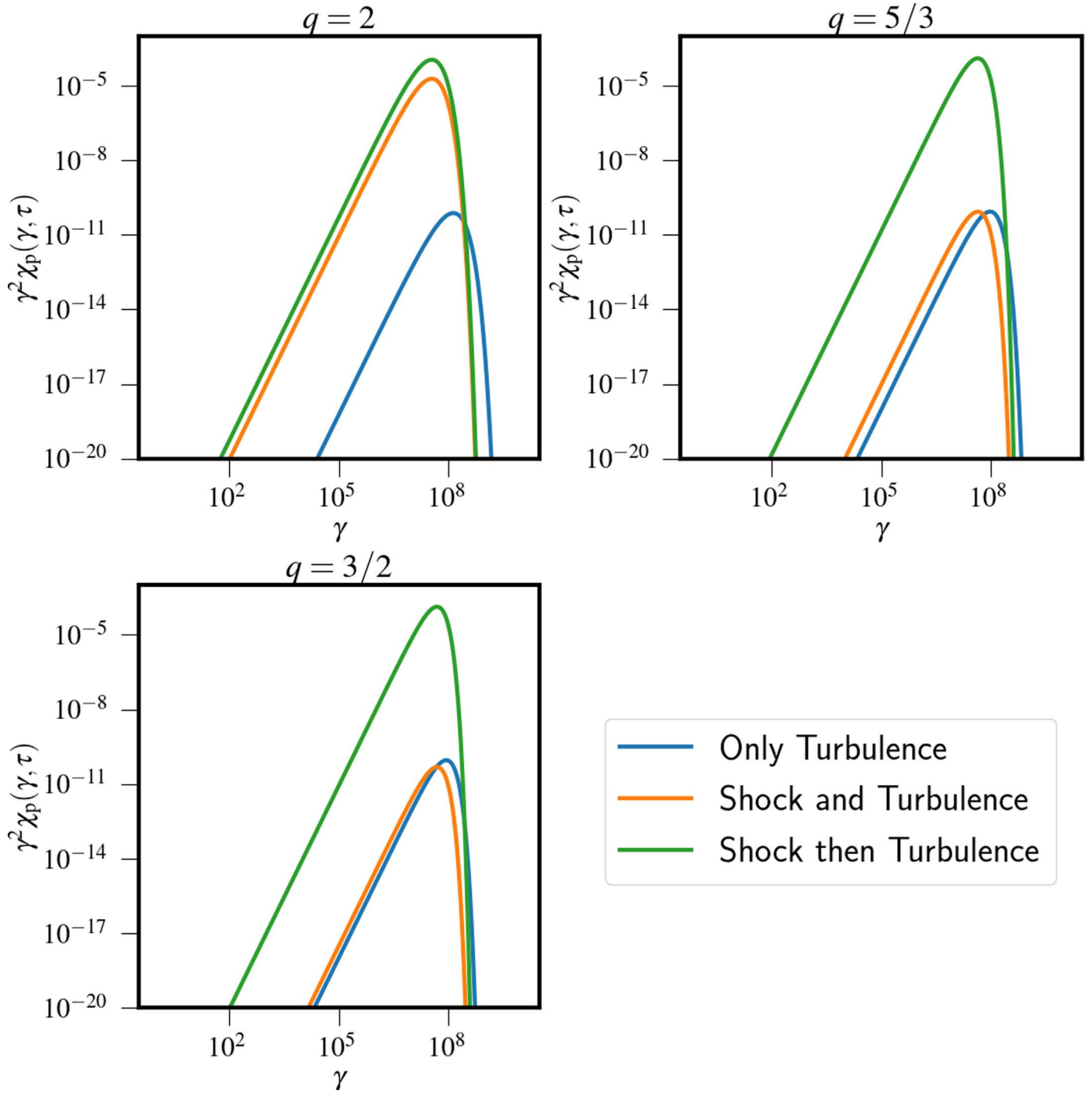

Figure 7. Steady-state particle distribution with shock and turbulence acceleration for various turbulence spectra. Top left: for $q = 2$; top right: for $q = 5/3$; and bottom: for $q = 3/2$. The solid blue line depicts the case of turbulent acceleration without shock; the orange line describes the case of shock and turbulence acceleration considering that both regions ahead of and behind the shock are turbulent; and the green line describes the shock and turbulence acceleration scenario in which only the post-shock region is turbulent.

analytic form (Equation (37)). We observe a good correspondence between the results.

5.1.2. Interplay of DSA and STA

In the previous section we found that the shock acceleration depends on the upstream spectrum. With this motivation here we try to analyze the impact of STA on particle shock energization by modulating the acceleration timescale t_A and display its effect on the shock injection with different compression ratios. Moreover, we define the value of t_A in terms of t_L at $\gamma = 1.0$ and for each choice of t_A, we perform the simulation up to time $\tau = 100\,\hat{\tau}_0$. Owing to the conserving nature of the boundary condition, the number of microparticles in a macroparticle remains the same once the shock takes place, thus by calculating the number of microparticles after the shock we estimate the effect of shock injection when STA is in process. The variation of the total number of particles after the

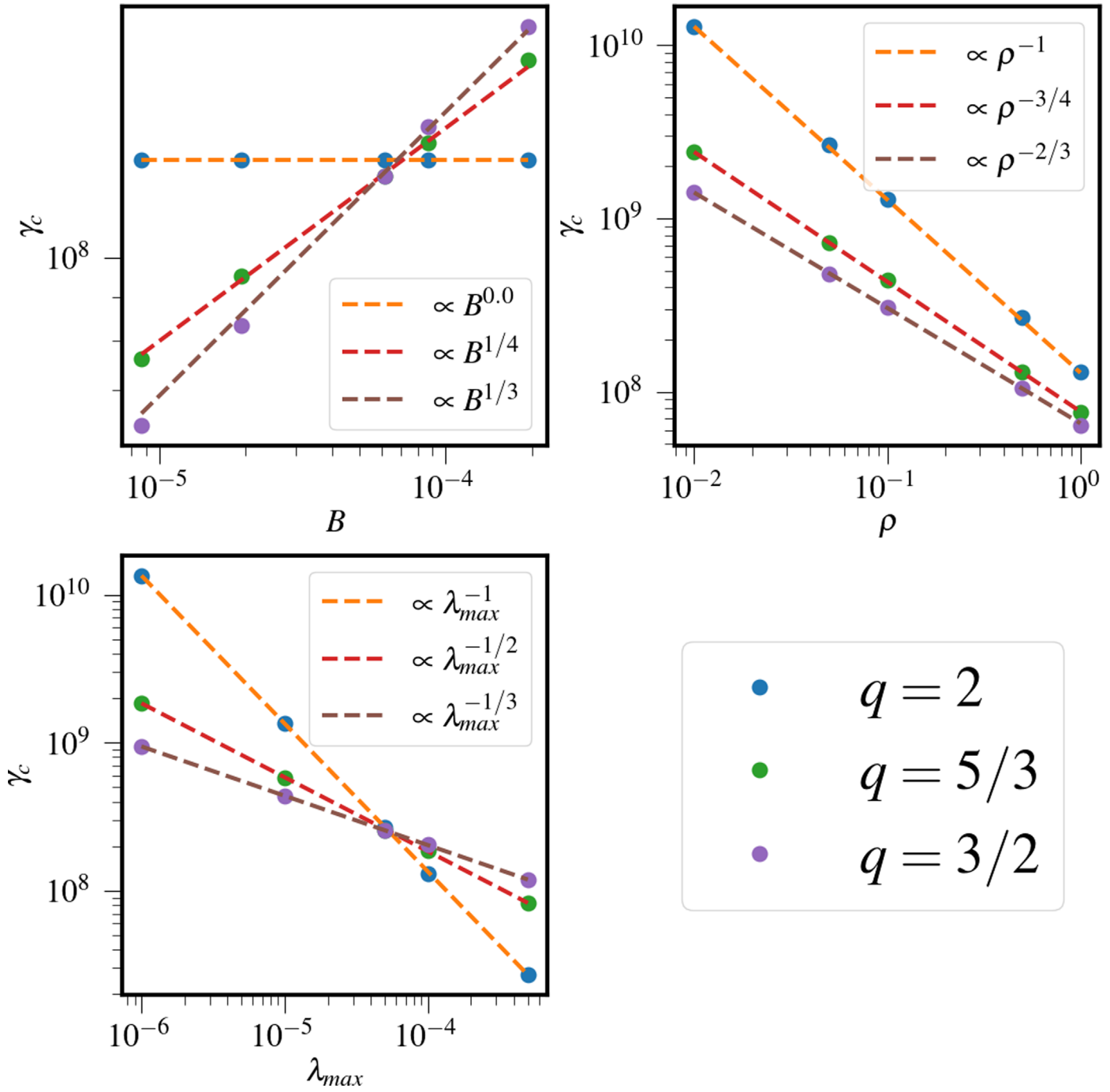

Figure 8. Dependence of γ_c on various parameters for turbulent acceleration. Left: dependence of γ_c on various B fields. Middle: dependence of γ_c on various ρ values. Right: dependence of γ_c on various values of $\lambda_{\rm max}$. Data point from corresponding simulations are shown as dots and the result from the analytic calculations (see Equation (37)) are shown with dashed lines for reference.

shock is shown with the ratio t_A/t_L at $\gamma = 1.0$ for different shock compression ratios in Figure 9 with a fixed magnetic field calculated using $\beta = 100.0$. Furthermore, the corresponding particle spectra at $\tau = 100\ \hat{\tau}_0$ are plotted for two values of the ratio and are shown in the insets of Figure 9.

When t_A is much less than t_L at $\gamma = 1.0$ (or the ratio t_A/t_L is small) the particle spectrum reaches the log-parabolic steady state (see section. 5.1), before the shock hits the particle, making the shock injection less effective. However, when the ratio t_A/t_L is comparatively high, one observes a very minute effect of STA on the particle distribution in the upstream, making the shock injection very effective for this case. Furthermore, notice that for any value of t_A/t_L a shock with higher compression ratio injects a greater number of particles than do the lower ones. Also from the distribution functions shown in the inset, for two different values of t_A/t_L, it can be observed that the spectra that were hit by a strong shock (high compression ratio) reach to steady state much faster compared with the spectra hit by a moderate shock (moderate compression ratio). Moreover, the decrement of the γ_c (see Section 5.1.1) with increasing t_A/t_L can also be seen. Additionally, the number can be seen to achieve a steady state

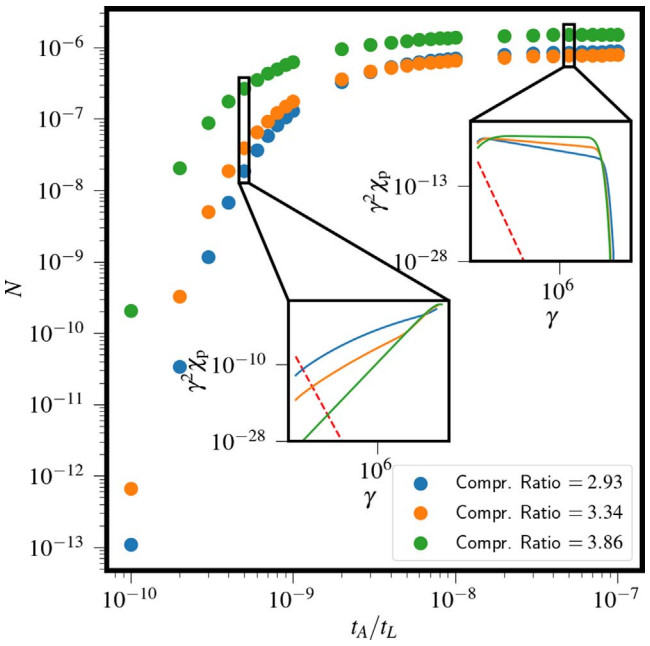

Figure 9. Dependence of shock injection on the upstream spectrum for various shock compression ratios with $\beta = 100.0$. The obliquity is made fixed at 30°. In the insets, the downstream distribution function is shown for two different values of t_A/t_L.

around $N \sim 10^{-6}$ at the higher values of t_A/t_L, which implies an upper bound of the particle injection at the shock for different compression ratios.

In summary, we observe that the effect of shock injection on the particle distribution function depends on the nature of the upstream particle distribution spectra. If the timescale of the STA in the upstream region is such that the particle distribution converges to steady-state spectra before the DSA can take place, the effect of shock injection becomes minimal. However, if in the upstream region the particle spectra do not reach the steady state before the shock hits the particle, then a considerable effect of shock injection on particle spectra can be seen. This analysis spans a wide parameter base and therefore showcases the interplay of these two particle acceleration processes.

5.2. Relativistic Blast Wave

Here, we focus on the impact of a relativistic blast wave on the evolution of the spectral distribution in the presence of both a shock and turbulence. Due to the underlying symmetry of the problem we choose a single quadrant with 512^2 Cartesian computational zones with $x,\ y \in [0,\ 6]$. The initial condition consists of an overpressurized central region of circular radius $0.8\hat{L}_0$ filled with pressure and density $\{P_c,\ \rho_c\} = \{1,\ 1\}$ surrounded by a uniform medium with $\{P_e,\ \rho_e\} = \{3 \times 10^{-5},\ 10^{-2}\}$. The magnetic field is taken perpendicular to the $\{x,\ y\}$ plane, $\boldsymbol{B} = B_0\hat{z}$, as in Vaidya et al. (2018). The boundary condition is set to be reflecting at $x = y = 0$ and outflow elsewhere. We initially place 360 Lagrangian macroparticles uniformly over $0 < \phi < \pi/2$ at the radius of $\sqrt{x^2 + y^2} = 2$. Physical units are chosen such that $\hat{L}_0 = 10$ pc, $\hat{\rho}_0 = 0.01$ amu, $\hat{P}_0 = 1.5 \times 10^{-5}$ dyne cm^{-2}, $\hat{v}_0 = c$, $\hat{B}_0 = 1.37 \times 10^{-2}$ G, and $\hat{\tau}_0 = 32.64$ yr. The initial distribution function for each macroparticle is taken to be a steep decreasing power-law profile with index 9 covering a range in Lorentz factor $\gamma \in \{1,\ 10^8\}$ discretized using 128 bins. Similar to the MHD planar shock test (Section 5.1), the diffusion coefficient is modeled following the acceleration timescale and the losses are modeled following the synchrotron, inverse Compton, and adiabatic loss processes.

The evolution of the particle distribution for a macroparticle initially placed at 65° for $q = 2$ is shown in Figure 10, where the particle evolution is shown for three different magnetic fields: $B_0 = 5 \times 10^{-2}$ (left panel), $B_0 = 5 \times 10^{-3}$ (middle panel), and $B_0 = 5 \times 10^{-4}$ (right panel). Furthermore, in all three cases $\lambda_{\max} = \hat{L}_0/10$.

For the case with the strongest magnetic field, the particle distribution initially evolves due to STA and, after crossing the shock, a steady-state ultra-relativistic Maxwellian-like spectral distribution can be seen to emerge eventually with a sharp cutoff beyond $\gamma_c \sim 10^8$. By contrast, for the weakest magnetic field case, the spectral evolution shows distinct signatures of DSA only. Indeed, an STA signature can hardly be observed, as the timescale obeys $t_A \propto B^{-2}$ (see Equation (12)) and is thus very large for the simulation time. In this case, the initial steep spectra are accelerated and the spectral slope is flattened and cooling due to synchrotron and IC emission is evident from the cutoff. Moreover, it should be noted that the particle can be energized beyond $\gamma > 10^9$. For the intermediate case, we observe effects of both the shock and STA in shaping the particle spectra.

Additionally, we quantified grid orientation effects by estimating the slope of the distribution functions for each macroparticle as a function of their initial angular positions. This is shown, at time $\tau = 6$ for $B_0 = 5 \times 10^{-4}\hat{B}_0$, in Figure 11. The final slope for all of the macroparticles approximately falls in the same range (≈ -4) with additional variations due to the discretization error ($\sim$2%). Therefore all macroparticles will have a similar spectral distribution as shown for the typical macroparticle in Figure 10, apart from minor variations due to the discretization error.

5.3. Relativistic Magneto-hydrodynamic Jet

In this section, we describe a toy model of a relativistic MHD jet and analyze its emission signatures due to the DSA and STA of cosmic rays. In particular, we employ a 2D cylindrical grid $\{R,\ Z\} \in \{0,\ 0\}$ to $\{20,\ 50\}$ using 160×400 grid cells. The ambient medium is initially static ($\boldsymbol{V}_m = 0$) with constant density $\rho_m = 10^3\hat{\rho}_0$, where $\hat{\rho}_0 = 1.67 \times 10^{-24}$ gr cm^{-3}. An underdense beam with $\rho_j = \hat{\rho}_0$ is injected into the ambient medium with velocity v_z along the vertical direction through a circular nozzle of unit radius, $R_j = \hat{L}_0$, from the lower Z boundary. The value of v_z is prescribed using the Lorentz factor $\gamma_j = 10$ and $\hat{L}_0 = 100$ pc, implying an unit timescale of $\hat{\tau}_0 = 326.4$ yr. The magnetic field is purely poloidal, $\boldsymbol{B} = B_z\hat{\boldsymbol{e}}_z$, and is initially prescribed in a jet nozzle and also in the ambient medium,

$$B_z = \sqrt{2\sigma_z P_j}, \tag{38}$$

where P_j is the jet pressure at $R = R_j$ estimated from the Mach number $M = v_j\sqrt{\rho_j/(\Gamma P_j) + 1/(\Gamma - 1)} = 6$ and adiabatic index $\Gamma = 5/3$. The value for σ_z is taken to be 10^{-4} for the present simulation.

We further inject 25 Lagrangian macroparticles every two time steps with an initial power-law spectral distribution with

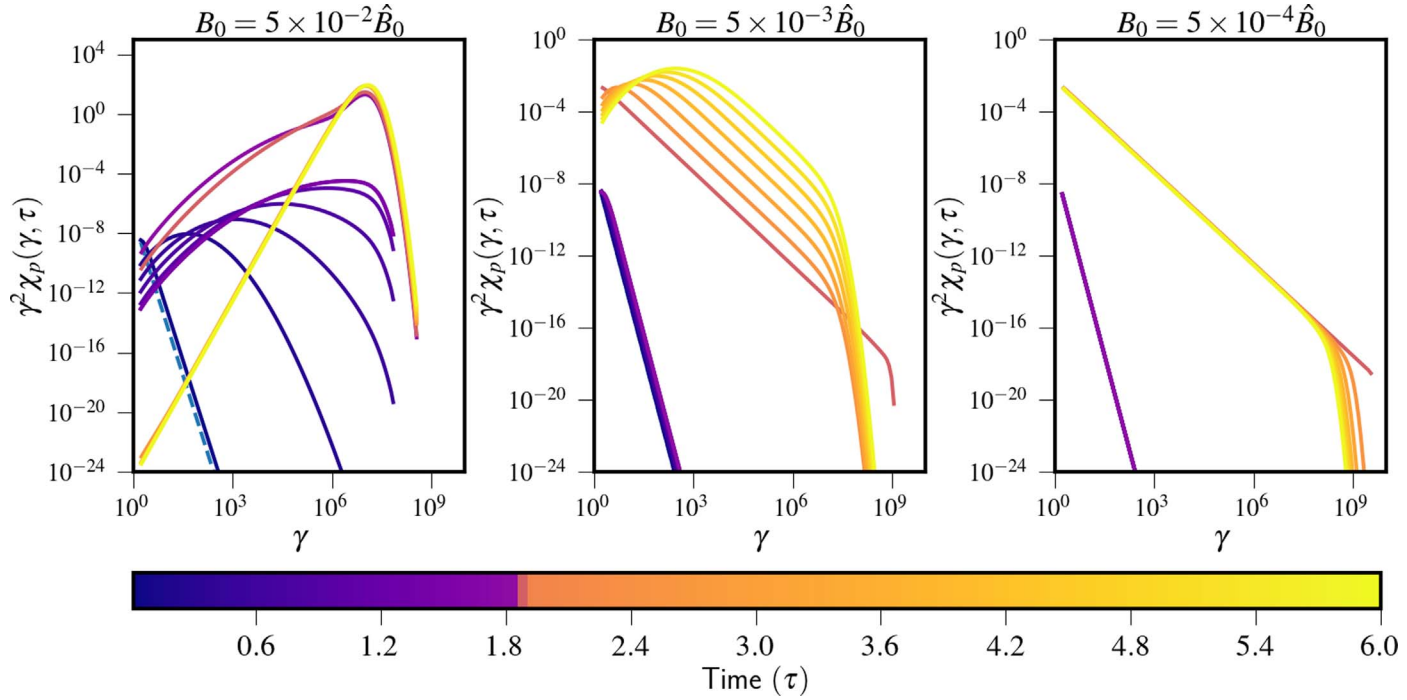

Figure 10. Temporal evolution of the particle distribution of a Lagrangian particle in a turbulent medium for a relativistic blast wave with different B fields. The turbulent spectrum is taken as $\propto k^{-2}$, so the value of q is 2 and $\lambda_{\rm max} = \hat{L}_0/10$. Left: for $B_0 = 5 \times 10^{-2}\hat{B}_0$; Middle: the evolution of the particle distribution for $B_0 = 5 \times 10^{-3}\hat{B}_0$. Right: the evolution for $B_0 = 5 \times 10^{-4}\hat{B}_0$. The dashed blue line corresponds to the initial distribution function, which is $\propto \gamma^{-9}$.

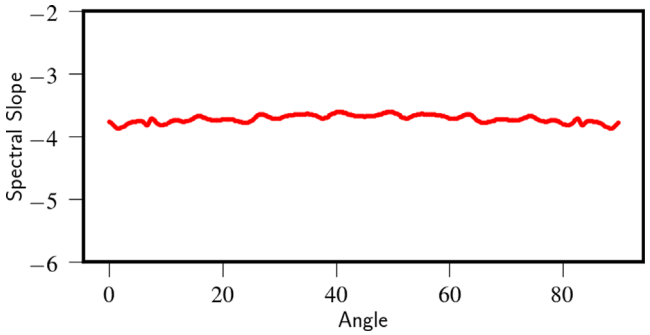

Figure 11. Spectral slope distribution of particles initially placed at different angle (ϕ) at the final time ($\tau = 6$) with $B_0 = 5 \times 10^{-4}\hat{B}_0$ for the relativistic blast wave test.

index -9 on an initial γ grid with $\{\gamma_{\rm min}, \gamma_{\rm max}\} \equiv \{1, 10^5\}$ discretized with 128 bins.

The energy spectra of the macroparticles are calculated for two different scenarios: (1) considering only DSA and different losses, and (2) considering, in addition, also stochastic processes. For scenario (1) we follow the numerical algorithm developed in Vaidya et al. (2018) and Mukherjee et al. (2021) to estimate the particle spectral distribution, while for scenario (2) we solve Equation (6) without the source and sink terms, along with the diffusion coefficient $D \propto \gamma^2$, where the proportionality constant is computed from the value of t_A following Equation (12) and with the value of $\lambda_{\rm max} = \hat{L}_0/100$. The loss terms account for synchrotron, IC, and adiabatic losses. Also, compared to the previous test problems here we take Courant number 0.8 when solving Equation (6). Moreover, for both scenarios we compute the emissivity for each macroparticle based on its local spectral distribution and interpolated it on the underlying grid (Vaidya et al. 2018).

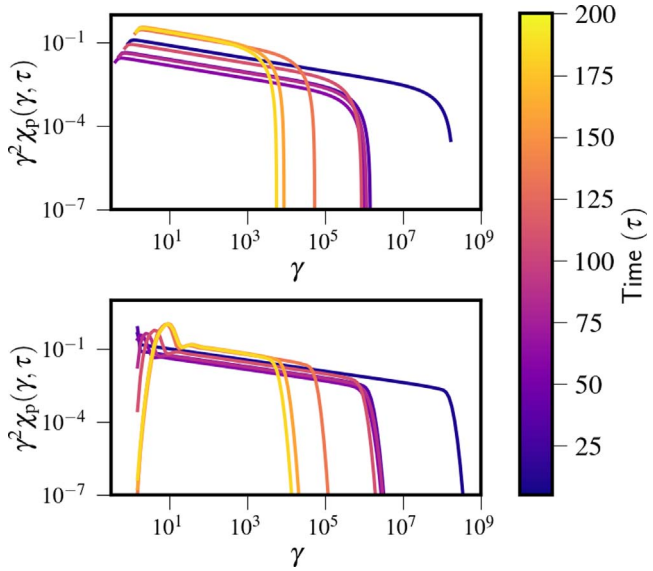

Figure 12. Temporal evolution of the spectrum of a Lagrangian particle that has gone through a shock at least once in the RMHD Jet. Top: for the case of only DSA; bottom: for the case of STA along with DSA.

In Figure 12, we show the spectral evolution of representative particles that have been shocked at least once for each of the scenarios. The top panel shows the spectral evolution of a representative particle for the case in which acceleration is due to shocks alone. The effects of DSA and radiative losses are clearly visible, respectively, from the spectral flattening and from high-energy cutoffs. Here, the cutoff can be observed clearly, as during DSA the maximum energy gets shifted according to the prescription described in Section 2. When the maximum γ exceeds its initial value, cooling processes become

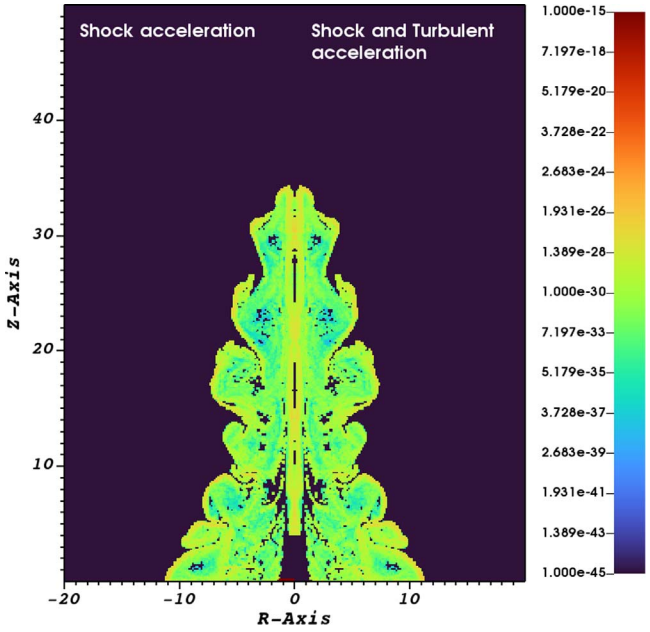

Figure 13. Comparison between the emission from turbulence and DSA and only DSA for radio frequency 1.4 GHz at time $\tau = 200$. Notice that the radial coordinate has been mirrored in the left plot.

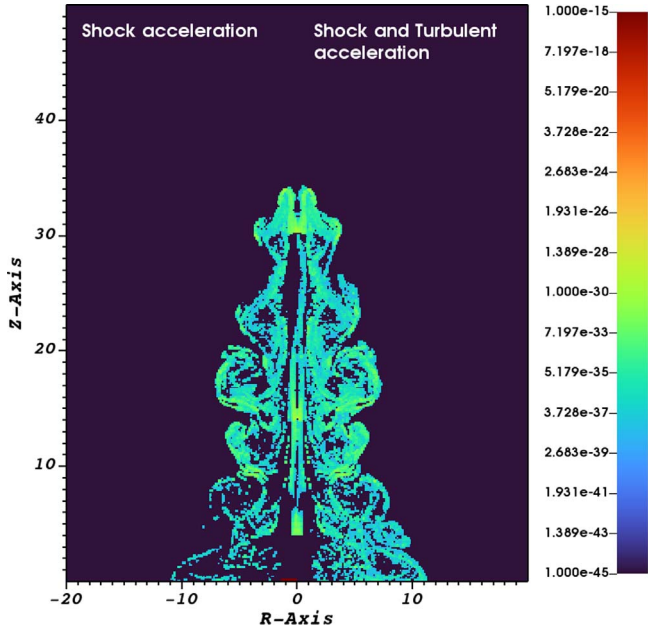

Figure 14. Same as Figure 13 but for optical blue light of frequency 6.59×10^5 GHz at time $\tau = 200$.

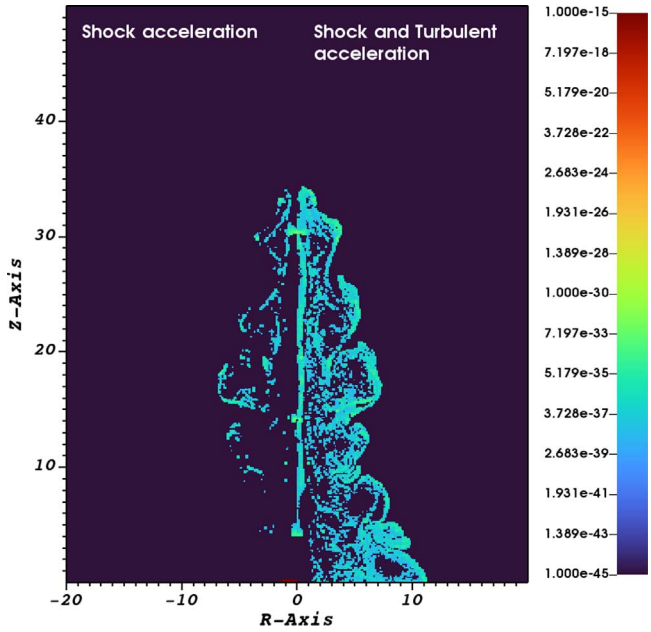

Figure 15. Same as Figure 13 but for 0.4 KeV X-ray emission at time $\tau = 200$.

effective so that the macroparticle quickly cools, accounting for the sharp spectral cutoff.

The bottom panel shows the spectral evolution of a similar particle for the case in which STA is also included (besides DSA). The distribution reveals a hump-like structure in the low-energy end of the spectrum that slowly shifts toward higher γ values. With time, this eventually causes the distribution function to reach a steady state, as described by Equation (A2). Notice that our choice of parameters (Equation (12)) is such that the acceleration timescale t_A is larger or comparable to the dynamical time, leading to feeble acceleration. We also point out that, during the initial stages, the particle spectrum exhibits a pile-up effect at low γ, because of the finite grid constraint, as discussed in Section 4.3. This spurious effect dims with time as lower γ particles start to accelerate toward higher γ. The impact of DSA (in addition to STA) can be distinguished from the flattening of the spectral distribution. The more pronounced low-energy cutoff is attributed to the lower energy particles being accelerated by STA, eventually creating a deficiency in the number of particles at low γ.

From the instantaneous spectral distribution of Lagrangian macroparticles spread across the computational domain, we estimate the synchrotron emissivity by convolving the macroparticle spectra with single electron synchrotron spectra and interpolated it on the computational grid (see Equations (36)–(37) in Vaidya et al. 2018). In Figures 13, 14 and 15, the emissivity J_ν computed from the Lagrangian macroparticles is shown for different frequencies at time $\tau = 200\hat{\tau}_0$ for the two different scenarios (left and right halves, respectively).

In Figure 13, at the 1.4 GHz radio frequency, the emission due to turbulence and the shock (the right half) is very similar to the case for DSA only (the left half). For the case with optical frequency ($\nu = 6.59 \times 10^5$ GHz; Figure 14), the emission becomes less than that at the radio frequency (Figure 13) for both cases with and without STA. This is expected because of the faster cooling time with higher energy. However, a significant larger emission can be seen in case (2) in the region $Z \lesssim 10$. The material in this region originates from the backflow dynamics of the jet (Cielo et al. 2014; Matthews et al. 2019). If only shock energization is accounted for, the particle spectra become very steep in this region owing to radiative losses and the absence of strong shocks. However, if STA is also taken into account, the spectra remain hard because of the competing effects of STA and radiative losses. Similar high emission features are observed in the X-ray ($\nu = 10^8$ GHz) as well (right panel of Figure 15). By contrast, in the presence of DSA only, a significant reduction in the X-ray emission can be seen (the left half). Here, most of the emission originates from the regions near the jet head as well as isolated spots in the cocoon. In addition, smaller emission centers can be observed in the region around the re-collimation shocks

along the beam. This differs from the case with DSA + STA, where the emission pattern is wider and more uniformly distributed throughout the jet and the backflow region.

6. Discussion and Summary

In this paper we have focused on the numerical modeling of STA and its physical contribution to the spectral evolution of highly energetic particles. The numerical formulation is based on the fluid−particle hybrid framework of Vaidya et al. (2018) and Mukherjee et al. (2021) developed for the PLUTO code, in which the nonthermal plasma component is modeled by means of Lagrangian macroparticles embedded in a classical or relativistic magnetized thermal flow.

The particle distribution function is evolved by solving numerically a Fokker–Planck equation in which STA is modeled by two components: a hyperbolic term describing the systematic acceleration (Fermi II) and a parabolic contribution accounting for random resonant interactions between particles and plasma turbulent waves. While Vaidya et al. (2018) presented a Lagrangian method for the solution of the Fokker–Planck equation in the presence of hyperbolic terms only, here we have introduced a novel Eulerian algorithm to account also for an energy-dependent diffusion coefficient $D \sim \gamma^2$ that can become stiff in the high-energy limit. To overcome the explicit time step restriction, the new method takes advantage of second-order Runge–Kutta Implicit-Explicit (IMEX) methods, so that hyperbolic terms (e.g., adiabatic expansion, radiative losses, and Fermi II) are treated explicitly, while parabolic terms (modeling turbulent diffusion) are handled implicitly.

Selected numerical benchmarks validated against analytical solutions and grid resolution studies demonstrate that our implementation has improved stability and accuracy properties when compared to previous solvers (see, for example, Chang & Cooper 1970; Winner et al. 2019). In addition, due to the presence of a boundary condition our algorithm respects physical constraints (for example, $\gamma \geqslant 1$) that are not always satisfied in the Lagrangian method (Vaidya et al. 2018; Mukherjee et al. 2021) with an evolving grid. STA modeling has also been validated against radiative synchrotron loss processes by studying the evolution of the curvature of particle spectrum (Tramacere et al. 2011).

With these motivations, we have studied the effect of STA as well as other energization processes on the particle spectrum in the presence of shocks using toy model applications. Such an interplay is commonly believed to operate in supernova remnants, AGN radio lobes, galaxy clusters, and radio relics.

As a first application example, we considered a simple planar shock in four different acceleration scenarios. We found that when STA and DSA both are considered, the former seems to affect the shock injection by changing the macroparticle distribution function. Further tests with different forms of the diffusion coefficient reveal a similar behavior. Additionally, we have also quantified the effect of the STA timescale on the radiative losses and its influence on the interplay with DSA. In particular, we observe that the effect of shocks on the particle distribution weakens with decreasing STA timescales. A similar interplay between DSA and STA was also evident in case of a spherical shock formed in the test case of an RMHD blast wave.

Finally, we have extended our algorithm to explore the emission properties of the axisymmetric RMHD jet using a toy model. We find a significant difference both in the evolution of the spectral distribution and the ensuing emission signatures due to the presence or absence of the STA process. In particular, inclusion of STA results in diffuse emission within the jet backflow, particularly in the high-energy X-ray band. The consequences of such an important finding will be further explored in forthcoming works focusing on astrophysical systems along with comparison with observed signatures.

We would like to thank the anonymous referee for the helpful comments, and constructive remarks on this manuscript. S.K. and B.V. would like to thank the financial support from the Max Planck partner group award at Indian Institute of Technology, Indore. All simulations were performed at the computing facility at Indian Institute of Technology, Indore.

Appendix
Analytical Solution of Fokker–Planck Equation

Equation (6) is very hard to solve for a proper general analytic solution. Various works have been devoted to solve Equation (6) for various transport coefficients (e.g., Katarzyński et al. 2006; Park & Petrosian 1995; Chang & Cooper 1970; Kardashev 1962). Chang & Cooper 1970 solved Equation (6) for the steady-state solution and the solution can be written as

$$\chi_{\rm steady}(\gamma) = \chi_0 \exp\left\{-\int_1^{\gamma}\left(\frac{S(\gamma',\,\tau) - D_{\rm A}(\gamma',\,\tau)}{D_{\gamma\gamma}(\gamma',\,\tau)}\right)d\gamma'\right\}. \quad \text{(A1)}$$

Katarzyński et al. (2006) solved Equation (A1) for $D_{\gamma\gamma}(\gamma,\,\tau) = D_{\gamma 0}\gamma^2/2$ with $D_{\gamma 0} = 1/t_{\rm A}$, $D_{\rm A}(\gamma,\,\tau) = \gamma/t_{\rm A}$ and $S(\gamma,\,\tau) = S_0\gamma^2$. These forms of the parameters are typical for particles in plasma. The loss term $S(\gamma,\,\tau)$ gets a similar form if inverse Compton radiation is taken in the Thompson limit with Synchrotron radiation and the form for the diffusion coefficient $D_{\gamma\gamma}$ that also matches the form from a typical particle in cell simulations as discussed above. The solution to Equation (A1) with the above mentioned parameters is

$$\chi_{\rm steady}(\gamma) = \chi_0\gamma^2 \exp\{-2S_0 t_{\rm A}(\gamma - 1)\}. \quad \text{(A2)}$$

Kardashev (1962) got a time-dependent solution for Equation (6) without the loss terms and showed the acceleration leads to a log-normal particle distribution (similar to Equation (36)).

So, if the particles only accelerate via STA, the particle distribution follows a log-normal form due to the fact that the STA process is a multiplicative acceleration process (Tramacere et al. 2011). But if those particles lose their energy via radiative means along with the acceleration, the particle distribution starts to follow an ultra-relativistic Maxwellian distribution (Equation (A2)), which looks like a thermal or quasi-thermal spectrum with a scaled temperature of $1/S_0 t_{\rm A}$, which is also the value of γ where $t_{\rm A} = t_{\rm L}$.

ORCID iDs

Sayan Kundu https://orcid.org/0000-0003-3126-0588
Bhargav Vaidya https://orcid.org/0000-0001-5424-0059
Andrea Mignone https://orcid.org/0000-0002-8352-6635

References

Achterberg, A., & Krulls, W. M. 1992, A&A, 265, L13
Asano, K., & Hayashida, M. 2018, ApJ, 861, 31
Ascher, U. M., Ruuth, S. J., & Spiteri, R. J. 1997, ApNM, 25, 151
Bai, X.-N., Caprioli, D., Sironi, L., & Spitkovsky, A. 2015, ApJ, 809, 55

Baring, M. G. 2004, NuPhS, 136, 198
Baring, M. G., Ellison, D. C., & Jones, F. C. 1994, in IAU Coll. 142, ed. E. L. Chupp & A. O. Benz (Cambridge: Cambridge Univ. Press), 547
Bell, A. R. 1978, MNRAS, 182, 147
Bell, A. R. 2014, BrJPh, 44, 415
Belmont, R., Malzac, J., & Marcowith, A. 2008, A&A, 491, 617
Blandford, R., & Eichler, D. 1987, PhR, 154, 1
Blandford, R. D. 1994, ApJS, 90, 515
Borse, N., Acharya, S., Vaidya, B., et al. 2021, A&A, 649, A150
Böttcher, M., & Dermer, C. D. 2010, ApJ, 711, 445
Brunetti, G., & Lazarian, A. 2007, MNRAS, 378, 245
Bykov, A. M., & Fleishman, G. D. 1992, MNRAS, 255, 269
Chang, J., & Cooper, G. 1970, JCoPh, 6, 1
Cielo, S., Antonuccio-Delogu, V., Macciò, A. V., Romeo, A. D., & Silk, J. 2014, MNRAS, 439, 2903
Comisso, L., & Sironi, L. 2018, PhRvL, 121, 255101
Dermer, C. D., Miller, J. A., & Li, H. 1996, ApJ, 456, 106
Donnert, J., & Brunetti, G. 2014, MNRAS, 443, 3564
Drury, L. O. 1983, RPPh, 46, 973
Ellison, D. C., & Double, G. P. 2002, APh, 18, 213
Ellison, D. C., Jones, F. C., & Reynolds, S. P. 1990, ApJ, 360, 702
Ellison, D. C., Warren, D. C., & Bykov, A. M. 2013, ApJ, 776, 46
Fan, Z.-H., Liu, S., Wang, J.-M., Fryer, C. L., & Li, H. 2008, ApJL, 673, L139
Fermi, E. 1949, PhRv, 75, 1169
Ferrand, G., & Marcowith, A. 2010, A&A, 510, A101
Giacalone, J., & Ellison, D. C. 2000, JGRA, 105, 12541
Giacalone, J., & Jokipii, J. R. 1999, ApJ, 520, 204
Jokipii, J., Giacalone, J., & Kóta, J. 2007, P&SS, 55, 2267
Kang, H., Ryu, D., & Jones, T. W. 2017, ApJ, 840, 42
Kardashev, N. S. 1962, SvA, 6, 317
Katarzyński, K., Ghisellini, G., Mastichiadis, A., Tavecchio, F., & Maraschi, L. 2006, A&A, 453, 47
Kirk, J. G., Duffy, P., & Gallant, Y. A. 1996, A&A, 314, 1010
Kirk, J. G., Melrose, D. B., & Priest, E. R. 1994, in Plasma Astrophysics, ed. A. O. Benz & T. J.-L. Courvoisier (Berlin Heidelberg: Springer)
Kulsrud, R. M., & Ferrari, A. 1971, Ap&SS, 12, 302
Lemoine, M., & Pelletier, G. 2003, ApJ, 589, L73
Liu, S., Petrosian, V., & Melia, F. 2004, ApJL, 611, L101
Malkov, M. A., & Drury, L. O. 2001, RPPh, 64, 429
Marcowith, A., & Casse, F. 2010, A&A, 515, A90
Marcowith, A., Ferrand, G., Grech, M., et al. 2020, LRCA, 6, 1
Marcowith, A., & Kirk, J. G. 1999, A&A, 347, 391
Massaro, E., Perri, M., Giommi, P., & Nesci, R. 2004, A&A, 413, 489
Massaro, E., Tramacere, A., Perri, M., Giommi, P., & Tosti, G. 2006, A&A, 448, 861
Matthews, J. H., Bell, A. R., Araudo, A. T., et al. 2019, in Ultra High Energy Cosmic Rays 2018 (UHECR 2018), ed. I. Lhenry-Yvon et al. (Les Ulis: EPJ Web of Conferences), 04002
Meli, A., & Biermann, P. L. 2013, A&A, 556, A88
Melrose, D. B. 1996, Ap&SS, 242, 209
Mertsch, P., & Petrosian, V. 2019, A&A, 622, A203
Mignone, A., Bodo, G., Massaglia, S., et al. 2007, ApJS, 170, 228
Mignone, A., Bodo, G., Vaidya, B., & Mattia, G. 2018, ApJ, 859, 13
Mimica, P., & Aloy, M. A. 2012, MNRAS, 421, 2635
Miniati, F. 2001, CoPhC, 141, 17
Miniati, F. 2003, MNRAS, 342, 1009
Miniati, F., Ryu, D., Kang, H., & Jones, T. W. 2001, ApJ, 559, 59
Mukherjee, D., Bodo, G., Rossi, P., Mignone, A., & Vaidya, B. 2021, MNRAS, 505, 2267
Niemiec, J., & Ostrowski, M. 2006, ApJ, 641, 984
Nishikawa, K.-I., Hededal, C. B., Hardee, P. E., et al. 2007, Ap&SS, 307, 319
Ostrowski, M. 1988, MNRAS, 233, 257
O'Sullivan, S., Reville, B., & Taylor, A. M. 2009, MNRAS, 400, 248
Palmroth, M., Ganse, U., Pfau-Kempf, Y., et al. 2018, LRCA, 4, 1
Pareschi, L., & Russo, G. 2005, JSCom, 25, 129
Park, B. T., & Petrosian, V. 1995, ApJ, 446, 699
Park, B. T., & Petrosian, V. 1996, ApJS, 103, 255
Parker, E. N. 1955, PhRv, 99, 241
Perri, S., & Zimbardo, G. 2015, ApJ, 815, 75
Petrosian, V. 2012, SSRv, 173, 535
Press, W. H., Teukolsky, S. A., Vetterling, W. T., & Flannery, B. P. 1992, Numerical Recipes in C: The Art of Scientific Computing (2nd edn.; Cambridge: Cambridge Univ. Press)
Rajpurohit, K., Hoeft, M., Vazza, F., et al. 2020, A&A, 636, A30
Rangelov, B., Montmerle, T., Federman, S. R., Boissé, P., & Gabici, S. 2019, ApJ, 885, 105
Rieger, F. M., & Duffy, P. 2019, ApJ, 886, L26
Sarazin, C. L. 1999, ApJ, 520, 529
Schlickeiser, R. 1989, ApJ, 336, 243
Schlickeiser, R. 2002, Cosmic Ray Astrophysics (Berlin: Springer)
Schlickeiser, R., & Dermer, C. D. 2000, A&A, 360, 789
Sironi, L., & Spitkovsky, A. 2011, ApJ, 726, 75
Spitkovsky, A. 2008, ApJ, 682, L5
Sturrock, P. A. 1966, PhRv, 141, 186
Teraki, Y., & Asano, K. 2019, ApJ, 877, 71
Tramacere, A., Massaro, E., & Taylor, A. M. 2011, ApJ, 739, 66
Tverskoĭ, B. A. 1967, JETP, 25, 317
Vaidya, B., Mignone, A., Bodo, G., Rossi, P., & Massaglia, S. 2018, ApJ, 865, 144
Vaidya, B., Prasad, D., Mignone, A., Sharma, P., & Rickler, L. 2017, MNRAS, 472, 3147
Van Leer, B. 1977, JCoPh, 23, 276
van Weeren, R. J., Andrade-Santos, F., Dawson, W. A., et al. 2017, NatAs, 1, 0005
Vazza, F., Wittor, D., Brunetti, G., & Brüggen, M. 2021, A&A, 653, A23
Vurm, I., & Poutanen, J. 2009, ApJ, 698, 293
Webb, G. M. 1989, ApJ, 340, 1112
Winner, G., Pfrommer, C., Girichidis, P., & Pakmor, R. 2019, MNRAS, 488, 2235
Wolff, M., & Tautz, R. C. 2015, A&A, 580, A58
Wong, K., Zhdankin, V., Uzdensky, D. A., Werner, G. R., & Begelman, M. C. 2020, ApJL, 893, L7
Zimbardo, G., & Perri, S. 2017, NatAs, 1, 0163